

Interpreting LSTM prediction on Solar Flare Eruption with Time-series Clustering

Hu Sun¹, Ward Manchester², Zhenbang Jiao¹, Xiantong Wang², Yang Chen^{1,3}

¹Department of Statistics

²Climate and Space Sciences and Engineering

³Michigan Institute for Data Science

Key Points:

- We present deep learning models to classify weak and strong first flares using SDO/HMI SHARP parameters calculated along the active region polarity inversion line.
- We demonstrate a dimension reduction technique to directly interpret the predictions of deep learning models and do variable selection to find threshold values for SHARP parameters that precede strong solar flares.
- We identify 35 active regions whose deep learning prediction scores for M/X class flares transition from very low to very high level.
- We demonstrate the key dynamics of SHARP parameters that drive such deep learning prediction performance.

arXiv:1912.12360v1 [astro-ph.SR] 27 Dec 2019

Abstract

We conduct a post hoc analysis of solar flare predictions made by a Long Short Term Memory (LSTM) model employing data in the form of Space-weather HMI Active Region Patches (SHARP) parameters. These data are distinguished in that the parameters are calculated from data in proximity to the magnetic polarity inversion line where the flares originate. We train the the LSTM model for binary classification to provide a prediction score for the probability of M/X class flares to occur in next hour. We then develop a dimension-reduction technique to reduce the dimensions of SHARP parameter (LSTM inputs) and demonstrate the different patterns of SHARP parameters corresponding to the transition from low to high prediction score. Our work shows that a subset of SHARP parameters contain the key signals that strong solar flare eruptions are imminent. The dynamics of these parameters have a highly uniform trajectory for many events whose LSTM prediction scores for M/X class flares transition from very low to very high. The results suggest that there exist a few threshold values of a subset of SHARP parameters when surpassed could indicate a high probability of strong flare eruption. Our method has distilled the knowledge of solar flare eruption learnt by deep learning model and provides a more interpretable approximation where more physics related insights could be derived.

1 Introduction

The Sun exhibits a wide range of eruptive activity, flares, filament eruptions and coronal mass ejections (CMEs), all of which are magnetically driven (see reviews by Forbes (2000); Schrijver (2009); Schmieder et al. (2015); Green et al. (2018)). The magnetic free energy driving these eruptions accumulates in the corona in association with electric currents (e.g. Janvier et al. (2014); Schmieder et al. (2015)). In response to these currents, the non-potential magnetic fields are sheared and twisted as seen in the structure of hot loops observed in the extreme ultraviolet (EUV). Such EUV images of pre-event corona often show bright loops with sigmoidal structure (e.g. Canfield et al. (1999); Magara and Longcope (2003); Aulanier et al. (2010); Green et al. (2011)), which are often harbingers of solar eruptions (Falconer et al., 2000).

In order to study and predict solar eruptions, one would ideally measure the magnetic field where eruptions occur, however the coronal magnetic field is difficult to deduce and impossible to localize beyond the plane of the sky (Dove et al., 2011). In contrast, spectropolarimetry of bright optically-thick spectral lines can provide high-resolution high-cadence reconstruction of the photospheric vector magnetic field in active regions where solar eruptions occur. Examination of magnetic fields has shown signatures strongly associated with solar eruptions that are indicative of increases in free magnetic energy such as: intensification of the horizontal magnetic fields (Wang et al., 2017), strong magnetic gradients (Schrijver, 2007), increases in magnetic shear (Georgoulis et al., 2012; Sun et al., 2012) increases in magnetic twist (Su et al., 2008; Vemareddy et al., 2012) and increases in magnetic and current helicities (Tziotziou et al., 2012; Wang et al., 2018). From these strong associations, predictive parameters and empirical relationships have been derived which are useful for predicting solar flares (e.g. Falconer et al. (2002, 2003); K. D. Leka and Barnes (2003a, 2003b); Falconer et al. (2006); Schrijver (2007)). These works tend to focus on flares because they are much more easily observed and categorized by energy level than either filament eruptions or CMEs.

Empirical relationships for predicting solar flares are now being surpassed by the application of machine learning made possible the the recent availability of vast quantities of magnetogram data. The most notably source is photospheric vector magnetograms from the Helioseismic and Magnetic Imager (HMI) instrument on the Solar Dynamics Observatory launched in February 2010 (Schou et al., 2012; Hoeksema et al., 2014). The first example of machine learning employing these data is that of Bobra and Couvidat

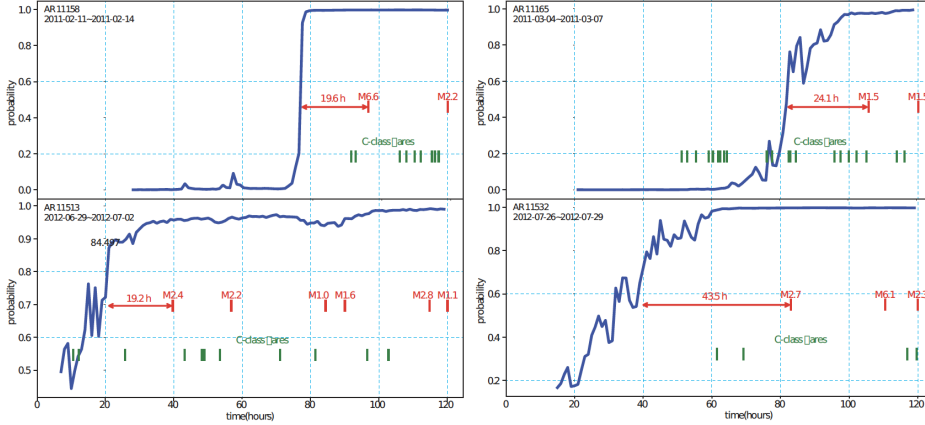


Figure 1. Four examples of prediction scores from the LSTM Strong/weak flare classification model first presented in Chen et al. (2019). Line plots show the probability of an M/X class flare occurring during a 12 hour interval extending into the future for active regions 11158, 11165, 11513, and 11532. Red and green marks indicate the occurrence M/X and class flares respectively.

(2015), which was followed by work such as Liu et al. (2017); Nishizuka et al. (2017); Huang et al. (2018); Chen et al. (2019), which used SHARP parameters for model training. In their work, Muranushi et al. (2016) and Nishizuka et al. (2018) developed deep neural networks for flare prediction. A description of these and related work is found in reviews by K. Leka and Barnes (2018) and Camporeale (2019).

Our work builds upon that of Chen et al. (2019), which used time-series SHARP parameter information for distinguishing strong solar flares of M/X class from weak flares of A/B class with the help of Long-Short-Term-Memory (LSTM) model. The LSTM model in Chen et al. (2019) takes a multi-dimensional time-series of all SHARP parameters as input and outputs a prediction score between 0 and 1. Scores close to 1 indicate that the time-series input contains strong signals of an M or X class solar flare. Chen et al. (2019) presented a few case studies (see Figure 1) where the LSTM prediction score (probability of seeing an M/X flare) increases abruptly prior to an M or X class flare, from nearly 0 to almost unity in a few hours.

This rapid change in the flare prediction score shows a strong sensitivity to the input data, which may suggest interpretation of the model may provide insight into conditions necessary for solar flares. Our prior work did not provided a detailed explanation of the signals contained in the LSTM inputs during these periods that drive such an abrupt change. Here we apply rigours mathematical analysis of these predictive models to determine the characteristics of the SHARP parameters time series most associated with the high probability of M- and X-class solar flares.

The LSTM model is a very promising machine learning tool for processing time-series data, but its internal structure is not simple enough for statisticians to give interpretations of a fitted model. The sudden transition of the prediction score of LSTM model provides a unique opportunity to discern the nature of the SHARP parameters that so strongly affect the flare prediction, which can then provide insight and understanding of solar flare eruptions. In particular, what is the essential differences of LSTM model inputs before and after the abrupt changes shown in the case studies in Figure 1? This leads us to a post hoc analysis on interpreting the trained LSTM model.

Discussions on interpretable machine learning models have been ongoing for more than a decade, and many recently proposed methods (Lundberg and Lee (2017)) consider interpreting black-box machine learning model in a model-agnostic way. Basically, people still treat the trained machine learning model as a black-box, and by permuting the inputs, adding noises to inputs, one could measure feature importance of the inputs by looking at how much the machine learning prediction performance changes. But these approaches are still not intuitive enough to derive enough domain-specific insights, especially when the machine learning model uses temporal data for training. In Chen et al. (2019), they used similar model-agnostic way to measure the feature importance in solar flare predictions by training LSTM model using only 1 SHARP parameter at a time and checking how much the prediction accuracy has dropped compared to the LSTM trained with all SHARP parameters, which is still far from satisfactory for explaining the phenomenon in Figure 1.

In this paper, we propose a more direct interpretation of the fitted LSTM model of a binary classification task where the LSTM is trying to learn to distinguish first M/X flare against first B flare of an active region. To improve interpretability, we train a similar LSTM model as that in Chen et al. (2019) but we use the SHARP parameters calculated along the polarity inversion line only. And instead of doing the interpretation in a model-agnostic way, we directly compare the LSTM model inputs, namely the multi-dimensional SHARP parameters, that produce low and high LSTM prediction scores.

Our idea is close the one of clustering analysis with sparsity (Witten and Tibshirani (2010)). One could think of all LSTM inputs with very low prediction scores as coming from a cluster in the feature space and all LSTM inputs with very high prediction scores as coming from another cluster. The feature space is spanned by all SHARP parameters. If we could find a few SHARP parameters that could cluster LSTM inputs in such a way that low-score LSTM inputs are clustered together and well separated from high-score LSTM inputs, these selected SHARP parameters would be the important SHARP parameters in LSTM prediction.

The technical challenge is that LSTM inputs for solar flare prediction are in a matrix shape, with one dimension being different SHARP parameters and the other being the temporal dimension. We propose a method to project all LSTM input matrices into a lower-dimensional space with the idea of using dynamic time warping. We found a single dimension in this low dimensional space where low and high prediction score cases are well separated. This enables us to explain the sudden transitions of LSTM scores seen in Figure 1, and more generally what SHARP parameters are more associated with the occurrence of strong solar flares.

In the next section, we will provide details about the SHARP parameter dataset along the polarity inversion line (PIL), and how we prepare train and test data for LSTM model. Section 3 revisits the theory of Long-Short-Term-Memory (LSTM) model and also provides the results of LSTM model based on the SHARP parameters along the PIL. In section 4, we outlined how we interpret LSTM predictions based on the idea of clustering, and showed case studies that fully explained the key SHARP parameters that are closely related to strong solar flare eruption. Section 5 concludes.

2 Data Preparation

Our machine learning model undertakes a first-flare classification task, which is the same as the task covered in Chen et al. (2019). The positive class is the first M or X flare while the negative class is the first B flare if any. The predictors used to classify these flares in Chen et al. (2019) are HMI photospheric vector magnetic field data associated with the flare region. These data are saved with a cadence of 12 minutes and resolution of 1 arc second (Hoeksema et al., 2014). From these data, subsets know as HMI Active

Region Patches (HARPs), are produced where data regions are spatially restricted to the near proximity of active regions (ARs). Furthermore, Space-weather HMI Active Region Patches, or SHARPs are an additional data product providing physical parameters calculated from the vector field, which are relevant to solar flare production, see Bobra et al. (2014) for detailed descriptions of these features. In this paper, we use the SHARP parameters that are calculated from vector magnetogram pixels along the polarity inversion line (PIL), with the detailed procedure of detecting PIL being discussed in Wang et al. (2019). This section introduces the PIL-based SHARP parameter dataset, the steps on how we collect the predictors and the overview of M, X, B first flares for training and testing the machine learning model. The SDO/HMI vector magnetic field images and SHARP parameters are available for download from Joint Science Operations Center (JSOC).

The polarity inversion line detection done in Wang et al. (2019) utilizes the method mentioned in Schrijver (2007). With the high-resolution vector magnetic field data of each HARP region, they first took the radial field, B_r , and produced two bitmaps, with one labelling all pixels satisfying $B_r > 200\text{G}$ as 1 and 0 otherwise, and the other labelling all pixels satisfying $B_r < -200\text{G}$ as 1 and 0 otherwise. Then they applied Density-Based Spatial Clustering of Application with Noise (DBSCAN; (Sander et al., 1998)) to cluster all strong positive pixels in the first bitmap and all strong negative pixels in the second bitmap. Finally, they applied Gaussian-Filter convolution to dilate the clusters of strong positive and negative pixels, and located the polarity inversion line as the intersection area of two dilated clusters of opposite polarity. The PIL mask generated is a weighted mask instead of a binary mask, which puts more weights on pixels that are close to both a strong positive polar and a strong negative polar. To calculate all the SHARP parameters from Table 3 in Bobra et al. (2014), excluding the ones related to Lorentz force, they multiplied the weighted PIL mask with the HMI vector magnetic field image pixel-wisely, and derived SHARP parameters based on the product image. See Figure 1 in Wang et al. (2019) for an example of the weighted PIL mask generated for HARP region 377.

The PIL-based SHARP parameters available are TOTUSJH, TOTPOT, TOTUSJZ, ABSNJZH, SAVNCP, USFLUX, AREA_ACR, MEANPOT, R_VALUE, SHRGT45, MEANSHR, MEANGAM, MEANGBT, MEANGBH, MEANGBZ, MEANJZH, MEANJZD, MEANALP, and with two extra parameters X_SIZE and Y_SIZE recording the width and height of each vector field image. The PIL-based SHARP parameters data is of 12 minutes cadence. Units of all physical quantities follow that in Table 3 of (Bobra et al., 2014). One caveat of interpreting the results related to any of these quantities is that all calculations of the physical quantities are weighted by the PIL-mask. For example, when a pixel's unsigned flux is added to the current USFLUX of the HARP region, the closer the pixel is to the PIL, the larger weight the flux of the pixel will have in the final calculation. This means that whenever we give a specific amount of any of the physical quantities, one should interpret the amount with a PIL mask in mind.

The flares we consider come from the NOAA Geostationary Operational Environmental Satellites (GOES) dataset, which has records of flares of various classes from mid 2010 to 2018. Among all the flares recorded for each NOAA active region in the GOES dataset, we focus only on the first M flare or X flare, whichever comes earlier, and the first B flare of each active region, if any. Then we assign each first flare to the corresponding HARP region, based on the mapping between NOAA active region number and HARP region number.

Since the PIL-based SHARP parameters are calculated based on vector magnetic field data of HARP regions, while the GOES dataset takes records of flares based on the NOAA active region number, there are some active regions with first M/X/B flares that do not have associated HARP region numbers, so our dataset do not contain these flares. Additionally, there are some HARP regions' B flares that happen after its first M/X flare, and those B flares are typically the last flares recorded for that HARP region. We only

want to focus on any B flares preceding the first M/X flare, so we discard those B flares samples. Eventually, we have only 681 first flares that have associated PIL-based SHARP parameters, among which there are 163 M/X flares and 518 B flares.

For each of the first flares of a certain HARP region, we gather all PIL-based SHARP parameters of that HARP region prior to the flare. Note that the length of the SHARP parameters time-series could vary from region to region since the recording time of different HARP regions prior to its first flare might differ. These first flares' PIL-based SHARP parameter data are the totality of the data we have prior to data pre-processing.

2.1 Machine Learning Input Data Collection

The machine learning model we use here is the Long-Short-Term-Memory (LSTM) model, which takes multi-dimensional time-series data as input. In the PIL-based SHARP parameters dataset, each solar flare has a preceding history of the SHARP parameters. We collect a 1-hour time-series of all these SHARP parameters 1 hour before each M/X/B first flare. See (a) of Figure 2 for an illustration on how we select the 1-hour input data.

Since the SHARP parameters is of 12 minutes cadence, a 1-hour time-series data contains 5 discrete time points for each of the SHARP parameters. In total we have 20 SHARP parameters (including X_SIZE and Y_SIZE), and we will use this 20×5 time-series data to classify the flare 1 hour later. Because we need to collect data from 2 hours before the flare till 1 hour before the flare, we need at least 2 hours of PIL-based SHARP parameters preceding a first flare. So we have to discard all flare samples which have less than 2 hours of SHARP parameters data preceding them.

In the vector magnetic field video preceding any first flares, there are certain cases where data in some frames are totally missing. We discard all the first flare samples whose preceding vector magnetic field video has more than 10% of its frames with missing data. For all the remaining samples with missing frames, we use linear interpolation to impute the missing values.

With all these data pre-processing, we finally obtain a flare list consists of 97 M/X flares and 305 B flares, with 402 flares in total. Table 1 provides a flare count summary for each year from 2010 to 2018.

Class/Year	2010	2011	2012	2013	2014	2015	2016	2017	2018	Total
M/X	0	15	12	20	27	18	3	2	0	97
B	2	53	48	52	23	46	52	23	6	305

Table 1. The number of M/X and B first flares recorded in each year in the dataset used for LSTM training and testing.

We label every M or X flare as 1, and every B flare as 0. There is only 1 X first flare happened in 2013 and all other 96 positive class flares are M flares, so we do not further distinguish M and X first flare, but choose to collapse the two classes into a single class. Our deep learning model will use the 20×5 SHARP parameters to give a prediction score between 0 and 1, and any score below 0.5 indicates a B flare and any score above 0.5 indicates an M/X flare.

With the trained model, we could select any 1-hour time-series SHARP parameter data preceding any first flare to give a prediction score. By sliding the 1-hour time window, we could produce a whole path of prediction scores along the entire time-series

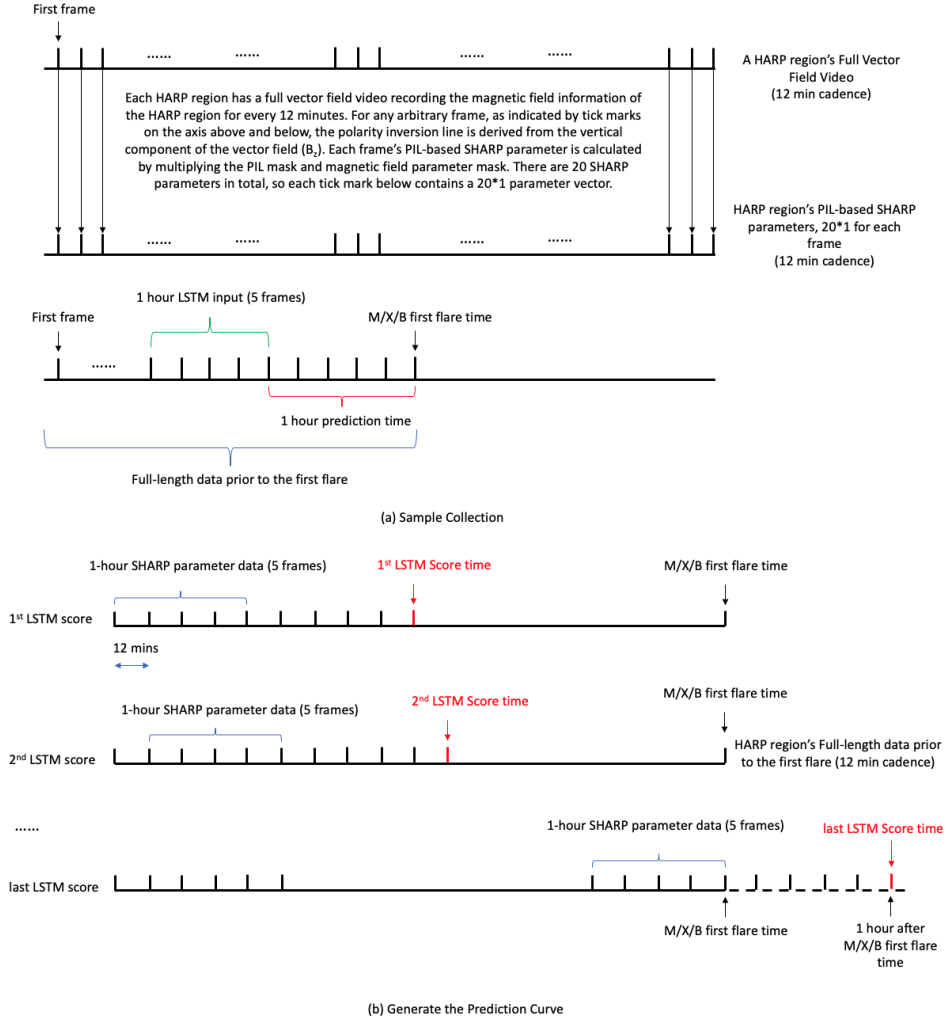


Figure 2. Schematic showing collection and distillation of data for input to train the LSTM and give the resulting predictions. All data are derived from a time series of three-component HMI vector magnetograms collected from the flare active region patches and saved at a 12 minute cadence. These are down-select to close proximity to the flare original site, the polarity inversion line (PIL). From these data, twenty physical scalar quantities relevant to flare production are calculated, the SHARP parameters. These data are then grouped together in one-hour, 5-frame sets, which are used to train the LSTM for flare classification, which provides the probability of an M/X flare 1 hour after.

prior to the first flare just as the one plotted in Figure 1. See (b) of Figure 2 for how we use the sliding window to collect 1-hour time-series data for every 12 minutes to generate a prediction score path.

The size of the dataset with 402 samples is comparable to the one used for first-flare classification in Chen et al. (2019), but with the PIL-based dataset, we have more localized features and a much less noisy SHARP parameter set, which could bring more interpretability when we analyze the patterns learnt by LSTM model.

2.2 Training/Testing Splitting and Normalization

The 402 flares in our dataset come from 369 different HARP regions, with only 33 HARP regions having both a first M/X flare and a first B flare. In order to give each HARP region's first flare a complete path of the LSTM classification score, we used the leave-one-out train-test set splitting.

Specifically, for each of the 369 HARP regions, we collect all its first flares and associated 1-hour predictor data and put them into the test set while all the other data in the train set. By doing so, we have 369 different ways of doing train-test set split.

To normalize each SHARP parameter to have mean zero and variance of one in each of these train-test set pair, we calculated the mean and standard deviation of each SHARP parameter of all samples in the train set only, and then normalize the test set with the mean and standard deviation coming from the train set to avoid any information leaking from the test set to the model training process. With the normalized data, we trained 369 LSTM models, each using one of the 369 train-test set pair. Eventually, the classification score path for each HARP region's first flares is generated with LSTM model trained with other HARP regions' first flare data only.

3 LSTM results and Sudden Transition

We apply Long-Short-Term-Memory(LSTM) model (Hochreiter & Schmidhuber, 1997) to classify first B flares and first M/X flares, and our model architecture follows that in Chen et al. (2019). This section detailed the deep learning neural network architecture and the results of the machine learning model.

3.1 Model Description

Long-Short-Term-Memory (LSTM) model is a special class of recurrent neural network (RNN), which is widely used to process sequential data such as time-series of stock prices and texts in twitters. It comes naturally in the application of solar flare prediction in that multi-dimensional time-series data, such as the SHARP parameters, are the typical predictors. RNN uses a recursive, highly non-linear mathematical operation to process the sequential inputs. The LSTM improves some of the drawbacks of traditional RNN by introducing a separate memory (called the cell state) to the neural network, where data of each time point in the time-series input could decide how much information the previous time points provided to the neural network can be kept for future use. This enables the information of data coming from the early stage to have an effect even after very long time. Figure 3 shows the tensor flows in our deep learning model consisting of LSTM cells.

Our neural network consists of two layers of LSTM. The first layer contains 5 LSTM cells chained together to process the 5 frames of SHARP parameters, namely X_1, X_2, \dots, X_5 and each X_i is a 20×1 vector. The input vector is processed by the nonlinear operations inside the LSTM cell and each cell outputs a memory $c_i^{<1>}$ and an output $h_i^{<1>}$ given the input vector X_i and the memory c_{i-1}^1 and output vector $h_{i-1}^{<1>}$ of the previ-

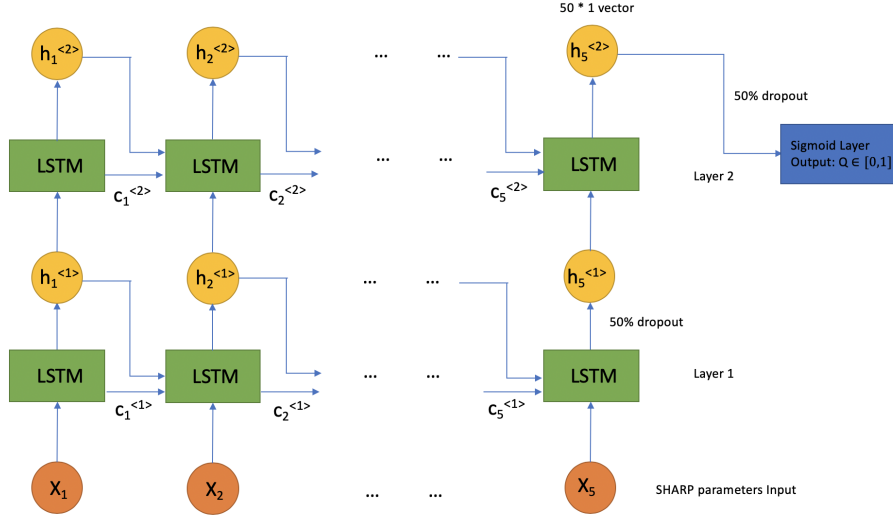


Figure 3. Two-layer LSTM architecture. X_1, X_2, \dots, X_5 are the 20×1 normalized SHARP parameters for each frame of the 1-hour input. $h_1^{<j>}, h_2^{<j>}, \dots, h_5^{<j>}, j = 1, 2$ are the outputs of each LSTM cell in the first and second layer. $c_1^{<j>}, c_2^{<j>}, \dots, c_5^{<j>}, j = 1, 2$ are the memory of each LSTM cell of the first and second layer. All memory and output vectors are 50. The output of each LSTM cell of the first layer, after a 50% random dropout, becomes the input of each cell of the second layer. The output vector from the last cell of the second layer, namely the $h_5^{<2>}$, is passed to a sigmoid function after 50% random dropout, and gives a prediction score between 0 and 1. The deep learning model is trained with binary cross-entropy loss to classify weak (B) and strong (M/X) flares.

ous cell. The memory and output vectors' dimensions can be tuned by the users. Here we specify the memory and output vector to be 50×1 vectors.

In the first layer, each LSTM cell's output $h_i^{<1>}$, after a 50% random dropout, becomes the input of the second layer of LSTM. The output of the last cell in the second layer, namely the $h_5^{<2>}$, which is a 50×1 vector, goes through 50% random dropout and is passed to a sigmoid function to give a score between 0 and 1.

Because we have 369 HARP regions in the first-flare classification task, and we have 369 different train-test set combinations, with each of the test set containing only first flares from a single HARP region, we have to train 369 LSTM models shown in 3. With each trained model, we could give a complete prediction score path for the HARP region in the test set, and we call the generated prediction score path the **leave-one-out prediction score**.

Figure 4 shows the leave-one-out prediction score and two SHARP parameters prior to the first M flare of AR 12017 and 12381. The unit of total free energy density (TOT-POT) is $\text{erg} \cdot \text{cm}^{-1}$, and the unit of mean shear angle (MEANSHR) is degree. But note that in the PIL-based dataset, all SHARP parameters are calculated under a weighted scheme. The total free energy density is the sum of all pixels' free energy density, weighted by each pixel's proximity to the detected polarity inversion line. The mean shear angle is the the sum of all pixels' shear angle, weighted by each pixel's proximity to the detected polarity inversion line, and then divided by the number of all non-zero pixels in

the PIL mask. Such a way of calculating the parameters make all SHARP parameters' magnitude not directly comparable to the full-image SHARP parameters.

We could see that the red curve (prediction score) and the blue curve (SHARP parameters) have some non-negligible positive correlations. The case for AR 12017 represents the type of prediction score path with abrupt changes. It can be seen that starting from the midnight of March 28, 2014, the prediction score suddenly increased to a very high level in a few hours, together with the sudden increase of both features. It can be easily inferred that the polarity inversion line emerged in a rather short period for AR 12017. During March 26th to 28th, both SHARP parameters stay at zero because the vector field during this period has no polarity inversion line.

Each black dot in the figure represents a flare event. Their logarithm-transformed intensity are shown on the axis "log flare intensity". The same intensity scale applies to all similar graphs in the following sections. For the sake of formatting simplicity, we do not draw the log flare intensity axis in the following graphs. It also can be seen that the SHARP parameters and prediction scores are higher when a stronger flare is upcoming.

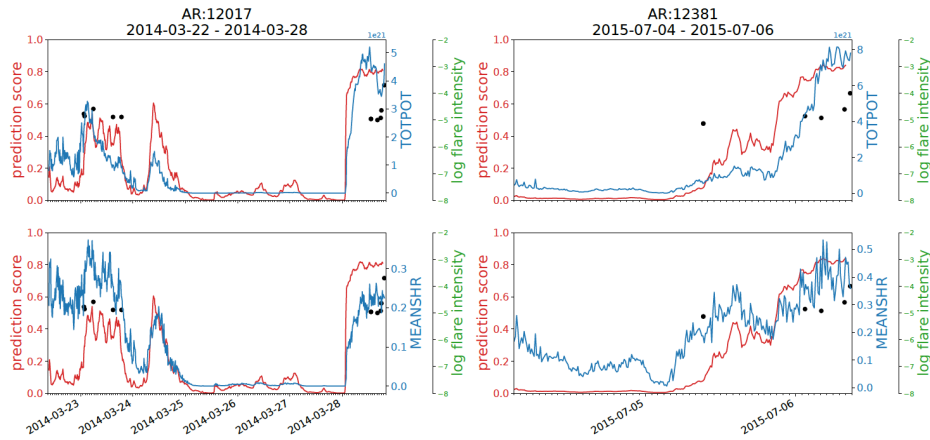


Figure 4. Prediction scores and key SHARP parameters plotted for AR 12017 and 12381 prior to their first M/X flare. Blue curve shows the time-series plots of TOTPOT and MEANSHR prior to the first M/X flare, red curve shows the leave-one-out prediction score. Each small black dots stands for a recorded flare event in GOES dataset for the active region. The height of the dot is proportional to the common logarithm of flare intensity, as can be found on the log flare intensity axis. Minor ticks on the time axis are plotted for every hour. The date format in the figure and all similar figures in the following text is Year-Month-Day. The unit of total potential energy (TOTPOT) is $\text{erg} \cdot \text{cm}^{-1}$, and the unit of mean shear angle (MEANSHR) is degree. Both SHARP parameters are weighted by the PIL-mask.

As for the case of AR 12381, the prediction score curve transitioned from relatively low level to relatively high level at a much slower pace. But it is common in both cases that the active regions have certain time with very low LSTM prediction score and other time with rather high LSTM prediction score. This LSTM prediction score path is actually a repeated observation for the HARP region, which makes it possible for us to contrast low and high LSTM score cases for a single HARP region. Instead of comparing AR 12017's SHARP parameters during its high LSTM score time against the SHARP parameters of AR 12381 during its low LSTM score time, it makes more intuitive sense for us to compare the SHARP parameters within an active region. So among all HARP

regions we are particularly interested in those that have both a low and a high LSTM score period like AR 12017 and 12381 and all regions in Figure 1 where inter-region comparison is possible. To give such a prediction score pattern a more formal definition, we define that an active region’s prediction score path has gone through a **sudden transition** if:

- An M/X flare happened at the end of the leave-one-out prediction score path.
- There is a certain time when the LSTM prediction score is above 0.7, and persist for at least 36 minutes afterwards. We call this time the **post transition time**.
- Prior to the post transition time, if there is any time when the LSTM prediction score is below 0.3, and persist for at least 36 minutes afterwards. We call this time the **prior transition time**.

Table A1 in the appendix provides all 35 cases where we found a sudden transition along their leave-one-out prediction score paths. Since the prediction score pattern for these active regions are quite similar which might indicate that the underlying physical processes can also be similar, the cases in the table can be used in other researches when one wants to give a uniform explanation for strong first flare eruption.

In all the cases in Table A1, the leave-one-out LSTM prediction score path has a certain time range where the prediction score jumped from a low level to a high level. Some of the transitions happened quickly, such as 12017 (2.5 hours) and 12182 (4 hours), but slower in cases such as 11718 (50 hours). Since all of the cases have gone through a significant LSTM prediction score change, it is possible for us to analyze whether there exists some within-region changes in some of the SHARP parameters that drive this score change and leads to the final M/X first flare. In the next section, we will provide a statistical technique to capture the driving force of high LSTM scores, and we will present case studies on these regions with sudden transitions to illustrate how certain SHARP parameters have changed significantly before and after the LSTM score transition.

4 LSTM Interpretation

Our method for interpreting the LSTM prediction is closely related to the idea of clustering analysis. Clustering analysis is the task of grouping a set of objects in such a way that objects in the same group (called a cluster) are more similar (in some sense) to each other than to those in other groups (clusters). In our machine learning setting, we want to cluster our LSTM model inputs, namely the SHARP parameters time-series, in a certain way such that inputs that produce low LSTM prediction score are more similar to each other than to those inputs that produce high LSTM prediction score.

Such an idea presents us with a task of constructing an appropriate measure of ”similarity” between LSTM inputs. Note that LSTM model input is a 2-dimensional matrix, with one dimension being the feature dimension and the other being the temporal dimension. There are infinite ways of defining the similarity between two 2-d LSTM inputs, such as calculating the Frobenius norm of the differences of two LSTM input matrices. But this similarity measure is not very interpretable. In this paper, we restrict ourselves to account for the similarity along the temporal dimension only.

Mathematically, suppose that we have two 2-d LSTM input matrices \mathbf{X} and \mathbf{Y} , both having shape $p \times t$, with p being the number of features (20 SHARP parameters in our case) and t being the length of each feature’s time-series (5 frames in our case). We measure the similarity of \mathbf{X} and \mathbf{Y} row by row. Therefore, we only need to define a similarity measure between two time-series of length t . The similarity between \mathbf{X} and \mathbf{Y} , denoted as $\mathbf{d}(\mathbf{X}, \mathbf{Y})$, will then become a $p \times 1$ vector, with each dimension summarizing the similarity of a certain feature’s time-series in the two inputs.

Now suppose \mathbf{X} gives a very low LSTM score, say around 0.05, and \mathbf{Y} gives us a fairly high LSTM score, say around 0.95. Also suppose that there is a third LSTM input \mathbf{Z} that gives a score at 0.10. If we find that compared to $\mathbf{d}(\mathbf{X}, \mathbf{Z})$, there are a few dimensions in $\mathbf{d}(\mathbf{X}, \mathbf{Y})$ that become significantly different, the features corresponding to these dimensions might be the most important features that drive LSTM scores to become high.

To proceed, we firstly introduce a time-series similarity measure called the Dynamic Time Warping (DTW) distance metric, which enables us to construct $\mathbf{d}(\mathbf{X}, \mathbf{Y})$. Then we will analyze which dimensions of $\mathbf{d}(\mathbf{X}, \mathbf{Y})$ will become significantly different when the LSTM scores of \mathbf{X} and \mathbf{Y} are very different.

4.1 Dynamic Time Warping Feature Construction

Dynamic Time Warping (DTW) distance (Sakoe & Chiba, 1978) is a measure of similarity between any two 1-d sequential data, especially temporal data. It is widely used in situations such as speech recognition where speakers might have different talking speed in various recordings and gene expression time-series analysis where different biological processes might unfold with different rates. In general, it measures how similar two time-series are to each other: the smaller the DTW distance is, the more similar the two time-series are.

Figure 5 gives an illustration on how dynamic time warping works. In the left panel, there are two time-series (X and Y) with equal length. If one uses the Euclidean distance measure, one would calculate the distance between the two time-series based on the differences of each pair of points at each time point. Points of two time-series are paired at each time point. This can be problematic when the two time-series are similar but the time progressions are not synchronous. For example, time series Y has a stable upward-sloping trend at early time of the series while time series X has a similar trend but with a relatively longer increasing time, as suggested by the different end time (shown in red points) of the increasing trend of X and Y . Dynamic time warping optimized the way time points of the two time-series are paired so that the two increasing trend in the two time-series can be paired with each other. This is indicated by the pairing of points where two red points (end of increasing trend) are paired together. The DTW distance is based on the differences of this new pairing, which is different from the Euclidean distance metric.

In the right panel of Figure 5, the two time-series are plotted again, but with one (X) at the bottom and the other (Y) rotated and shown on the left. With any time point i from X and any time point j from Y , we could calculate the squared difference of the time-series values of the two points: $(X_i - Y_j)^2$. The matrix represents a pair-wise squared differences between any two time points, with one from X and the other from Y . Equivalent to the illustration in the left panel where the pairing of time points are optimized to account for asynchronous time evolution, dynamic time warping distance is calculated by finding a path from the lower-left corner to the upper-right corner in this "pairing cost" matrix such that one has the smallest aggregated squared differences along the path. The optimal path's coordinates specify the optimized pairing rule for the two time-series. The optimal path for the X and Y has been plotted in the matrix and is the same as the pairing shown in the left panel. The DTW distance between X and Y is simply the square root of the sum of the matrix elements along this path: $\sum_{k=1}^K (X_{i_k} - Y_{j_k})^2$, where there are K points along the path and each point's coordinate is (i_k, j_k) .

Generally speaking, DTW distance gives one a distance metric between any two time-series of any length. Compared with Euclidean distance, it can identify time-series that has similar trend but with asynchronous time evolution. A small DTW distance means that the two time-series have similar time evolution path, while a large DTW distance means the time evolution of one time-series is very different from the other's.

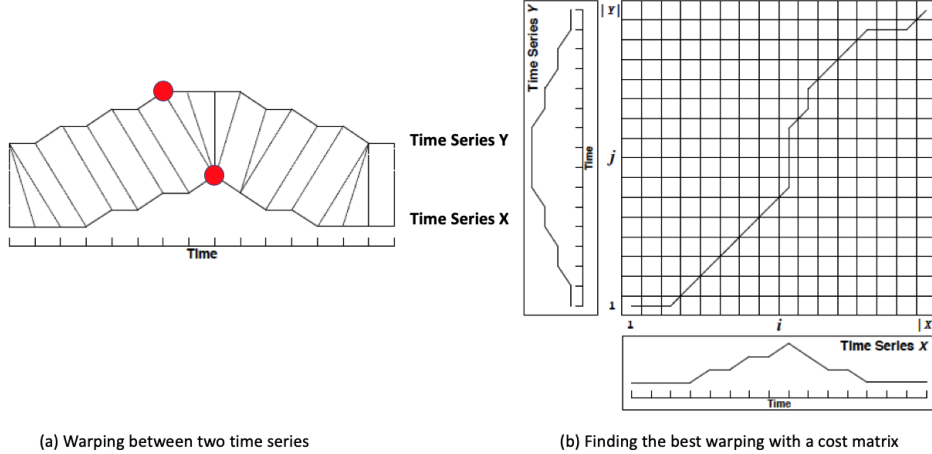


Figure 5. Explanation of Dynamic Time Warping. (a) shows the pairing of time points under the dynamic time warping distance measure. (b) shows that dynamic time warping is essentially a dynamic programming problem inside the pair-wise distance matrix of two time-series. Figures are adopted from Salvador and Chan (2007).

To apply DTW distance metric to the temporal dimension when comparing any two 20×5 inputs into the LSTM, we calculate the DTW distance between the time-series of each SHARP parameter. This gives us a 20×1 vector that summarized the time-series similarity between any two LSTM inputs for each SHARP parameter. (a) in Figure 6 illustrates the process for comparing two LSTM inputs at two arbitrary time points of a score path using dynamic time warping distance.

In our LSTM binary classification model, we have 402 flare samples in total and each has a leave-one-out prediction score path. Note that any single score on the score path corresponds to a 20×5 time-series input into the LSTM. We could compare any pair of points along a score path using the procedure described in Figure 6. Here, we choose to focus on contrasting inputs that produce high LSTM scores against inputs that produce low LSTM scores, so as to give insight into physical evolutionary trends leading to flare events. Consequently, for each score path, we search for the time point when the prediction score is the lowest as a **baseline point**. And for any time points along the score path, we calculate the corresponding DTW distance from the baseline point, which is represented as time point 1 in Figure 6. This point remains fixed so we only vary the time point 2 along the path. As a result, for each leave-one-out score path, we have constructed a 20 dimensional time-series of DTW distance of the 20 SHARP parameter. At each time point, the DTW distance measures how much the LSTM inputs at this time deviates from the LSTM input at the baseline time.

The essential idea of our LSTM interpretation is shown in (b) of Figure 6. Given the baseline point (shown in blue), we show several other points on the score path in a 2-d space where the coordinates are their TOTPOT and MEANSHR 1-hour time-series’s DTW distance from the baseline’s TOTPOT and MEANSHR 1-hour time-series. We hope to find a few variables that can linearly separate low and high LSTM score cases in the DTW distance space, such as the TOTPOT shown in (b).

In Figure 7, we showed the constructed DTW distance time-series of SHARP parameter total free energy density (TOTPOT) and mean shear angle (MEANSHR) for AR 12017 and 12381, along with their prediction score paths.

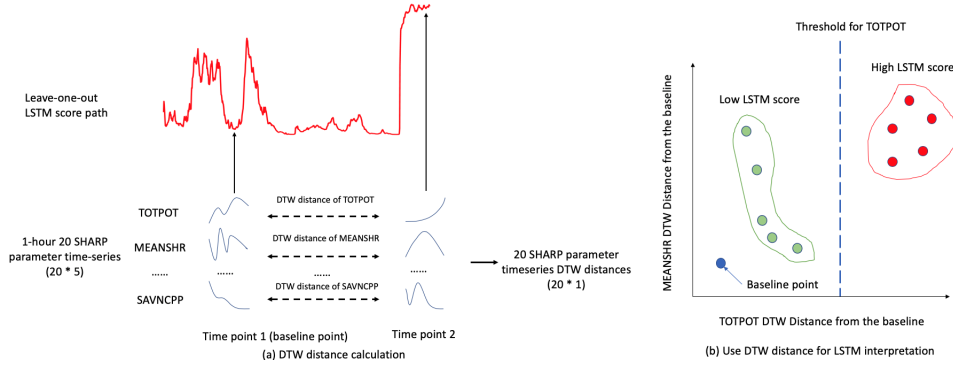


Figure 6. Illustration of how we use dynamic time warping distance to compare any two LSTM inputs and do interpretation. For any two arbitrary time t_1 and t_2 on the prediction score path of a certain HARP region, we collect their original 1-hour PIL-based SHARP parameter time-series \mathbf{X}_{t_1} and \mathbf{X}_{t_2} and calculate the DTW distance between each of the 20 SHARP parameter’s 1-hour time-series. Illustrations of the time profiles of parameters TOTPOT, MEANSHR and SAVNCP are provided. The final similarity between \mathbf{X}_{t_1} and \mathbf{X}_{t_2} is a 20-dimensional vector $\mathbf{d}(\mathbf{X}_{t_1}, \mathbf{X}_{t_2})$. In practice, we define a time point t_0 as the baseline point for the score path where the prediction score is the lowest along the path: $t_0 = \operatorname{argmin}_{\text{score}(t)}$. We then calculate the corresponding DTW distance between the LSTM inputs at any time point t and the baseline point t_0 . In (b), the baseline point is the blue point, and other time points’ DTW distances of SHARP parameter TOTPOT and MEANSHR against the baseline are plotted in a 2-d space. We aim to find the important variables of LSTM prediction by finding which variables could threshold low and high score inputs with the pattern shown in (b).

If one compares the curves of TOTPOT and MEANSHR in Figure 4 with the dynamic time warping distance features of the two SHARP parameters in Figure 7, one could see that the DTW distance features are smoother, have less local volatility and still have high correlation with the prediction score curve.

Using DTW distance metric enabled us to summarize the differences between inputs of the LSTM, but at the same time we may lose some high-order time-series information as the DTW distance is generally smoother than the original SHARP parameters. DTW distance captures the similarity of the general trend of two time-series. However, it puts less emphasis on the slope of the time-series. But we cannot neglect the slope information of SHARP parameters since they are present in the input of the LSTM. One cannot expect that the TOTPOT of AR 12017 and TOTPOT of 12381, who have different increasing speed, are processed in the LSTM similarly as they both started and ended up at similar magnitude.

Furthermore, we cannot neglect the different levels of local volatility of different SHARP parameters as well. As one can see from Figure 4, the MEANSHR of AR 12017 and 12381 are highly volatile during high LSTM score times, but the TOTPOT of AR 12381 is not as volatile. If we only focus on the mean and the slope of the SHARP parameters, we are not taking full considerations of how LSTM is going to handle these local perturbations. This requires us to compare the volatility of two LSTM inputs alongside comparing the general trend and slopes.

To better account for slope and local fluctuations of SHARP parameters, we used natural cubic spline (Hastie et al., 2001, Chapter 5) to interpolate each of 20 SHARP parameters of every active region, and then take the first-order derivative of the inter-

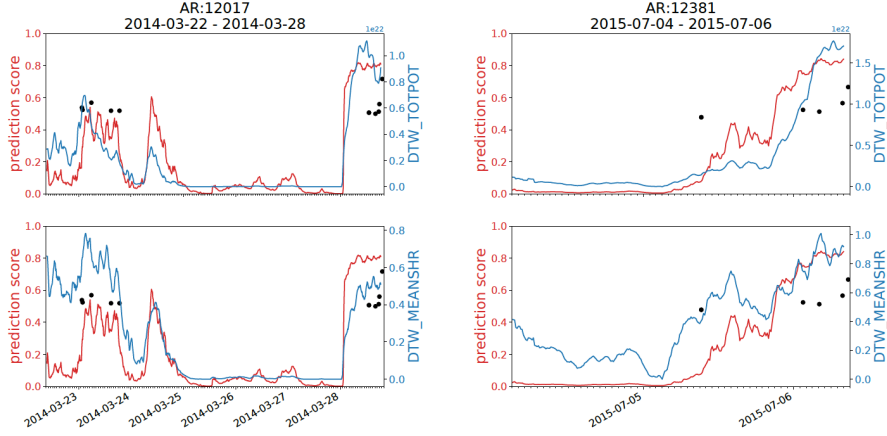


Figure 7. Prediction scores and DTW distance time-series of TOTPOT and MEANSHR for AR 12017 and 12381. Blue curve shows the time-series of DTW distance of SHARP parameter TOTPOT and MEANSHR prior to the first M/X flare, red curve shows the leave-one-out prediction score. Each small black dots stands for a recorded flare event. The height of the dot is proportional to the common logarithm of flare intensity, which is the same as that in Figure 4. Minor ticks on the time axis are plotted for every hour. Note the strong correspondence between the DTW distances and the prediction scores. The unit of DTW distance of total potential energy (TOTPOT) is $\text{erg} \cdot \text{cm}^{-1}$, and the unit of DTW distance of mean shear angle (MEANSHR) is degree.

polated curve to get each SHARP parameter’s first-order derivative time-series. Figure 8 shows the original MEANSHR and the derivative of MEANSHR of AR 12017 and 12381. Alongside the MEANSHR and derivative (MEANSHR_D), we also plotted the leave-one-out prediction score path and the moving 1-hour standard deviation of MEANSHR (1-hour local volatility of MEANSHR).

It can be seen that our spline fitting of the MEANSHR is capturing more about local volatility than slope of MEANSHR. When MEANSHR is increasing, we could see some significant non-zero derivatives in MEANSHR_D. But instead of giving a consistently positive derivative, the MEANSHR_D is fluctuating wildly around zero, with both strongly positive and strongly negative values. One can see that the magnitude of fluctuations of the MEANSHR derivatives is strongly correlated with the local volatility of the MEANSHR time-series. Most importantly, the MEANSHR fluctuates a lot when a solar flare is happening or about to happen, as one can see that MEANSHR_D is very volatile prior to flares with high intensity.

One may ask where does these local volatility come from? Given that the PIL-detection algorithm in Wang et al. (2019) does not account for the time-consistency of PIL across frames, but analyzes each vector field image at a time, we cannot expect that the PIL pixels found in one vector field image is the same as the PIL pixels found in the image 12 minutes later. The volatility of the SHARP parameters such as MEANSHR might come from the unstable PILs found in adjacent frames.

The other reason that might explain the volatility of SHARP parameters is the volatility of the vector field in HMI images. Each pixel’s magnetic field vector can change wildly for every 12 minutes. Therefore, even if we could find a stable PIL, we may have highly volatile SHARP parameters if the magnetic field changes a lot. These volatility that comes from the unstable PIL detection algorithm and the volatile HMI images will create sig-

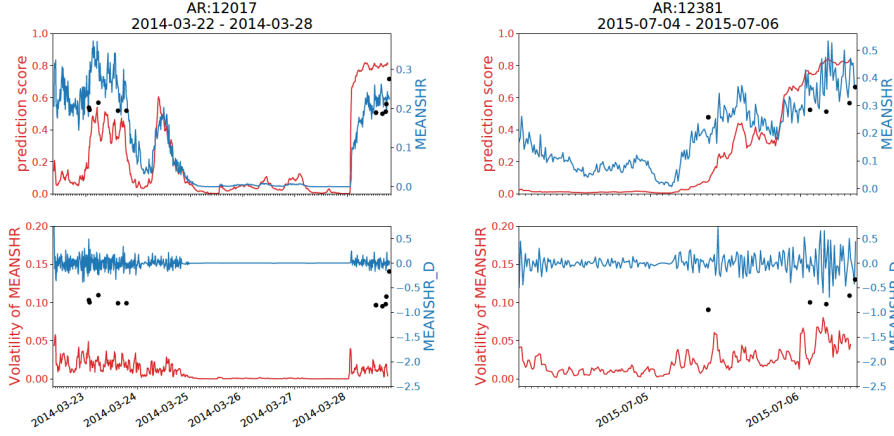


Figure 8. Plots of first-order derivatives of MEANSHR for AR 12017 and 12381. Blue curves show the time series of MEANSHR and its first-order derivative prior to the first M/X flare in the top and bottom panels respectively. Red curves show the leave-one-out prediction score and the 1-hour local standard deviation of MEANSHR in the top and bottom panels respectively. Each small black dots stands for a recorded flare event. The height of the dot is proportional to the common logarithm of flare intensity, which uses the same scale as that in Figure 4. Minor ticks on the time axis are plotted for every hour. There is a 3-day period for AR 12017 where the MEANSHR and MEANSHR_D are both constantly zero, this is because there is no polarity inversion line found during these time. Unit of mean shear angle (MEANSHR) is degree. Unit of derivative of MEANSHR is degree \cdot h $^{-1}$. Both parameters are weighted by the PIL-mask.

nificant local noises in the PIL-based SHARP parameters. Generally speaking, the SHARP parameters about the gradient of the magnetic field are more volatile while the parameters about the energy are smoother. Our spline fitting picks up local volatility for the gradient-related SHARP parameters and slope for the energy-related SHARP parameters.

To compare the slope and local volatility of SHARP parameters between LSTM inputs, similar to the DTW distance calculation implemented on 20 SHARP parameters, we calculated the DTW distance features of all 20 SHARP parameters' derivatives. Basically, for any 1-hour LSTM input, we calculate each SHARP parameter's derivatives. And we compute the DTW distance of these derivatives from the baseline point's derivatives. Consequently, we have 40 DTW distance features for each LSTM input, including 20 for original SHARP parameters and 20 for SHARP parameter derivatives. In Figure 9 we show the DTW distance features of the derivatives of TOTPOT and MEANSHR of AR 12017 and AR 12381. One can see that the DTW feature of the derivative of TOTPOT for AR 12381 is very smooth compared to all other 3 DTW features. This indicates that when a SHARP parameter has less local volatility, the derivative derived from spline mainly captures the slope of the time-series. When a SHARP parameter has more local volatility such as the MEANSHR, the derivative contains more of the local volatility information. Indeed, the discrepancy between the smoothness of TOTPOT and MEANSHR applies to many other pairs of SHARP parameters, and MEANSHR belongs to a certain group of SHARP parameters that are more volatile (gradient-related), while TOTPOT is a member of a group of SHARP parameters that are smoother (energy-related). More on the noises contained in SHARP parameters will be discussed in the following sections.

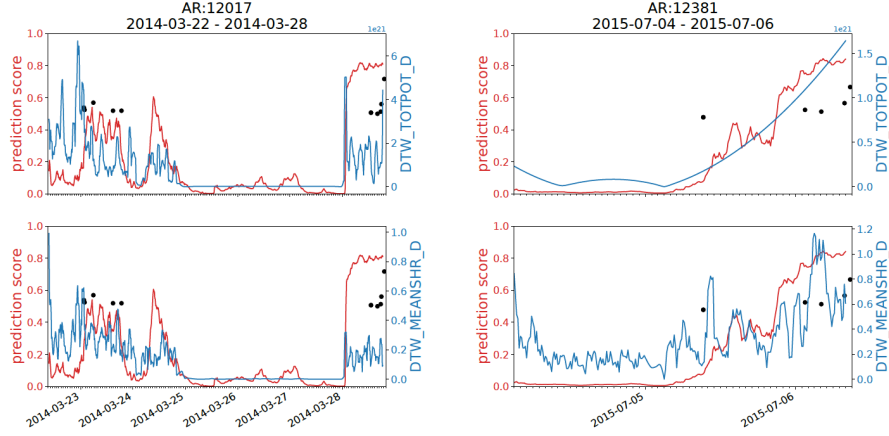


Figure 9. Plots of DTW distance for the first-order derivatives of TOTPOT and MEANSHR for AR 12017 and 12381. Blue curve shows the time-series of DTW distance of the derivatives of SHARP parameters TOTPOT and MEANSHR prior to the first M/X flare, red curve shows the leave-one-out prediction score. Each small black dots stands for a recorded flare event. The height of the dot is proportional to the common logarithm of flare intensity, which uses the same scale as that in Figure 4. Minor ticks on the time axis are plotted for every hour. We find a very close similarity between the evolution of the prediction scores and the DTW distance of the TOTPOT and MEANSHR variables’ time derivatives. Unit of the DTW distance of the derivative of TOTPOT is $\text{erg} \cdot \text{cm}^{-1} \cdot \text{h}^{-1}$. Unit of DTW distance of the derivative of MEANSHR is $\text{degree} \cdot \text{h}^{-1}$. Both parameters are weighted by the PIL-mask.

We did the DTW calculation for all of the 402 samples of our dataset. To avoid having an inappropriate baseline, we have discarded samples whose LSTM score of the baseline point is above 0.2. This is because we do not want our baseline point to have a very high prediction score, otherwise we are not contrasting other LSTM inputs with a low LSTM score baseline. After discarding all such samples, we still have 360 samples with inappropriate baseline, containing 70 M/X flares and 290 B flares. All 35 sudden transition cases are in these 360 samples.

Among all of the 40 DTW distance features, we are not interested in X_SIZE, Y_SIZE and their derivatives since they are constant over time and does not have physical interpretations. After deleting these 4 features, we finally got a set of 36 DTW distance features that summarized the similarity between any LSTM input of a HARP region and the baseline of that region.

In this subsection we introduced the concept of dynamic time warping (DTW) distance and have used this distance metric to compare different LSTM inputs. For each sample j with a leave-one-out prediction score path, we chose the time point with the minimum LSTM score as a baseline point. And for any LSTM inputs \mathbf{Y}_j that generates a score on sample j ’s score path, we measured the similarity between \mathbf{Y}_j and the baseline input \mathbf{X}_j using dynamic time warping for each SHARP parameter and their derivatives. Finally, we obtained a 36×1 DTW distance vector $\mathbf{d}(\mathbf{X}_j, \mathbf{Y}_j)$.

Among the 36 dimensions of this similarity metric, we have constructed two sets of DTW distance features, one about the original SHARP parameters and the other about the derivatives of the SHARP parameters. These two sets of DTW distance capture the similarity of the trend and the local volatility of the time-series input \mathbf{X}_j and \mathbf{Y}_j . A large

DTW distance of any SHARP parameter or its derivative at a certain time indicates that its time evolution has become significantly different from that of the baseline.

In the next subsection, we are going to analyze what has our first-flare LSTM classification model actually learnt. Specifically, we aim at identifying which dimensions in $\mathbf{d}(\mathbf{X}_j, \mathbf{Y}_j)$ have become significantly different when the LSTM score of \mathbf{Y}_j is very high, which is the idea shown in (b) of Figure 6.

4.2 A PCA analysis of DTW distance features

Figure 10 shows the Pearson correlation of these 36 DTW distance features across all 360 samples, with feature name ".D" representing the DTW distance feature of the derivative of a SHARP parameter.

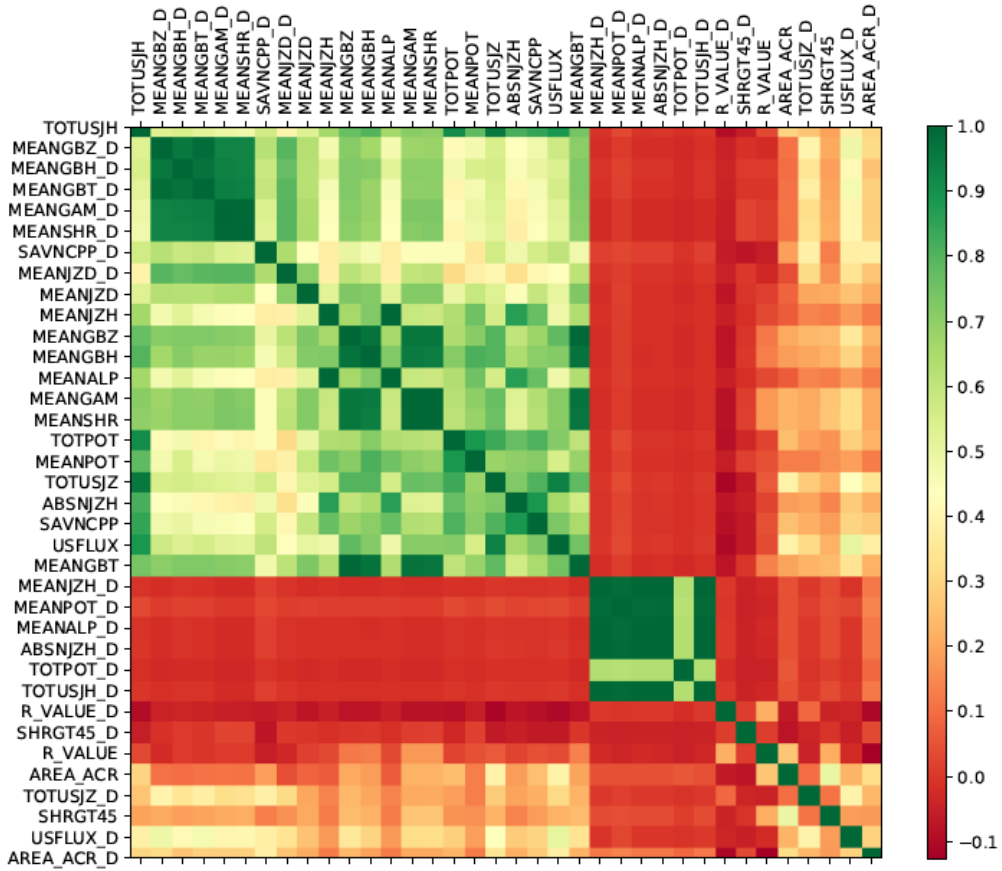


Figure 10. Pearson correlations among 36 DTW distance features. There are two highly correlated blocks, one consisting of the DTW feature of time derivatives of MEANGBZ, MEANGBH, MEANGBT, MEANSHR, MEANGAM, and the other including the time derivatives of MEANJZH, MEANPOT, MEANGALP, ABSNJZH, TOTUSJH. Furthermore, there is a weakly correlated block that includes more than 20 features on the top left corner of the correlation matrix (from TOTUSJH to MEANGBT). More quantitative description about the correlation structure can be found in Figure 11.

The correlation matrix shows that there is a large group of DTW distance features that are correlated with each other, as suggested by the large green block (from TOTUSJH

to MEANGBT) on the upper left corner. Specifically, MEANGBZ_D, MEANGBH_D, MEANGBT_D, MEANGAM_D and MEANSHR_D consist of a highly correlated block. The high correlation means that when the time evolution of some of the SHARP parameters or their derivatives become very different from the baseline of the HARP region, it is very likely that we observe the other highly-correlated features' time evolution to be very different from the baseline as well.

Recall that in Figure 7, the LSTM score path moves in the same direction with the DTW distance features of TOTPOT, MEANSHR. It seems that these two quantities could both have some predictive power on the LSTM score. So there is some overlapping information between these two dimensions of $\mathbf{d}(\mathbf{X}_j, \mathbf{Y}_j)$ in distinguishing low and high LSTM scores.

Indeed, if any dimension in $\mathbf{d}(\mathbf{X}_j, \mathbf{Y}_j)$ will become significantly different when the LSTM score of \mathbf{Y}_j is very high, we could expect all highly correlated dimensions to behave similarly. As a result of the correlation structure, we could analyze blocks of highly correlated DTW distance features instead of individual DTW distance features. And we applied principal component analysis (PCA) to do this dimension reduction to account for the shared information among the DTW distance features.

Principal component analysis (PCA) is a dimension reduction technique that uses orthogonal transformations to convert a set of observations of possibly correlated variables into a set of values of linearly uncorrelated variables called principal components. This transformation is defined in such a way that the first principal component has the largest possible variance, and each succeeding component in turn has the highest variance possible under the constraint that it is orthogonal to the preceding components. More details on PCA can be found in Bishop (2006, Chapter 12).

In our analysis, PCA will do eigenvalue decomposition of the Pearson correlation matrix in Figure 10. With PCA, we aim at finding out a few linear combinations of all 36 DTW distance features that can explain the variations of all 360 samples' DTW distance features.

Figure 11 shows the main results of PCA on DTW distance features. Panel (a) shows the proportion of variations explained by each of the 36 principal components, and (b), (c), (d) shows the feature loadings of the top 3 principal components. The first principal component (PC1) has large and relatively uniform loadings on all variables in the large green block on the upper left corner of Figure 10. So PC1 is a combination of all correlated DTW distance features of the large green block. When PC1 becomes large for a certain HARP region at some time, we could expect many of the features with large principal component loadings in PC1, such as TOTPOT and MEANSHR_D, have become significantly different from the baseline. PC2 captures the smaller dark green block of variables in the lower right corner, including DTW distance features of several SHARP parameters' derivatives. PC3 is a combination of many SHARP parameters' DTW features subtracting a group of other SHARP parameters' derivatives' DTW features.

One could regard the PC1 as the component containing the information of the changes of the mean structure of SHARP parameters' time evolution. PC2, as one may recall from Figure 9, contains the slope information of SHARP parameters such as TOTPOT, TOTUSJH and ABSNJZH, which are typically the less noisy SHARP parameters. And PC3, which turns out to be the most interesting principal component based on the post hoc analysis below, is the difference between the time evolution of the mean structure of parameters such as TOTPOT, ABSNJZH, SAVNCP and USFLUX and the volatility of MEANSHR, MEANGBZ, MEANGBH, MEANGAM, and MEANGBT. To put it simply, PC3 is to subtract noises of some SHARP parameters from signals of other SHARP parameters. One may note that some SHARP parameters' derivatives, such as MEANSHR_D, have large loadings in PC3 while its original parameter, such as MEANSHR,

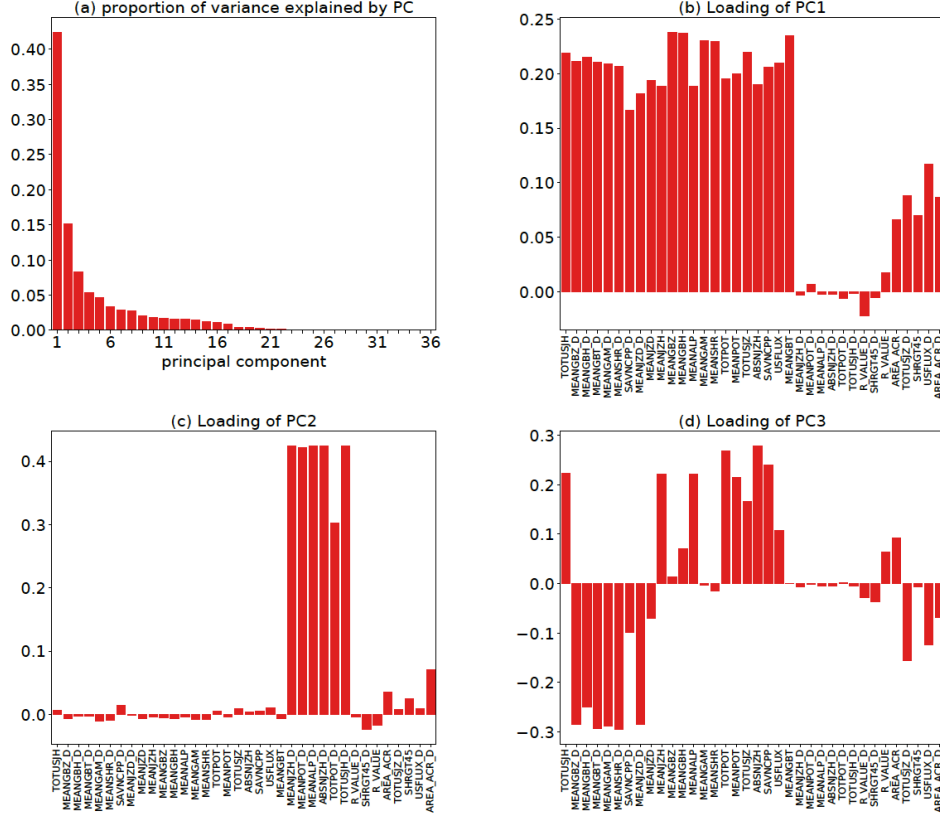


Figure 11. Results of Principal Component Analysis on 36 DTW distance features of 360 samples. The order of the variable of the graph on principal component loading is the same as Figure 10’s rows. (a) shows the proportion of variations explained by each of the 36 principal components of the PCA. (b), (c) and (d) shows the variable loadings of the first, second and third PCs with the largest eigenvalues. We found that PC1 captures the large green block in upper left corner of Figure 10, PC2 captures the small green block in the lower right corner and PC3 is the difference between variables highly correlated with TOTPOT and variables highly correlated with the time derivatives of MEANSHR.

have loadings near 0. In Figure 14, we will show, using some case studies, that MEANSHR may not be a SHARP parameter that can help one distinguish weak and strong flares while MEANSHR_D and TOTPOT can.

To check whether these principal components can distinguish low and high LSTM score cases, we calculated the 36 DTW distance features for 360 first-flare samples’ LSTM inputs, and then we calculated the 36 principal components scores of each LSTM inputs. In Figure 12, we plot all LSTM inputs whose LSTM prediction score is below 0.3 (blue) or above 0.7 (red), in a 2d space with the x-axis being their PC1 score and the y-axis being their PC3 score.

It can be seen that high LSTM score cases are typically those whose PC3 score is positive, and most are larger than 3. On the contrary, the low LSTM score cases are those with low PC3 scores. In terms of the PC1 score, even though there are many cases with high PC1 score from both classes, we could see that there are many cases with high LSTM score that have very large PC1 score, well beyond 20, which is rarely seen in low LSTM score cases.

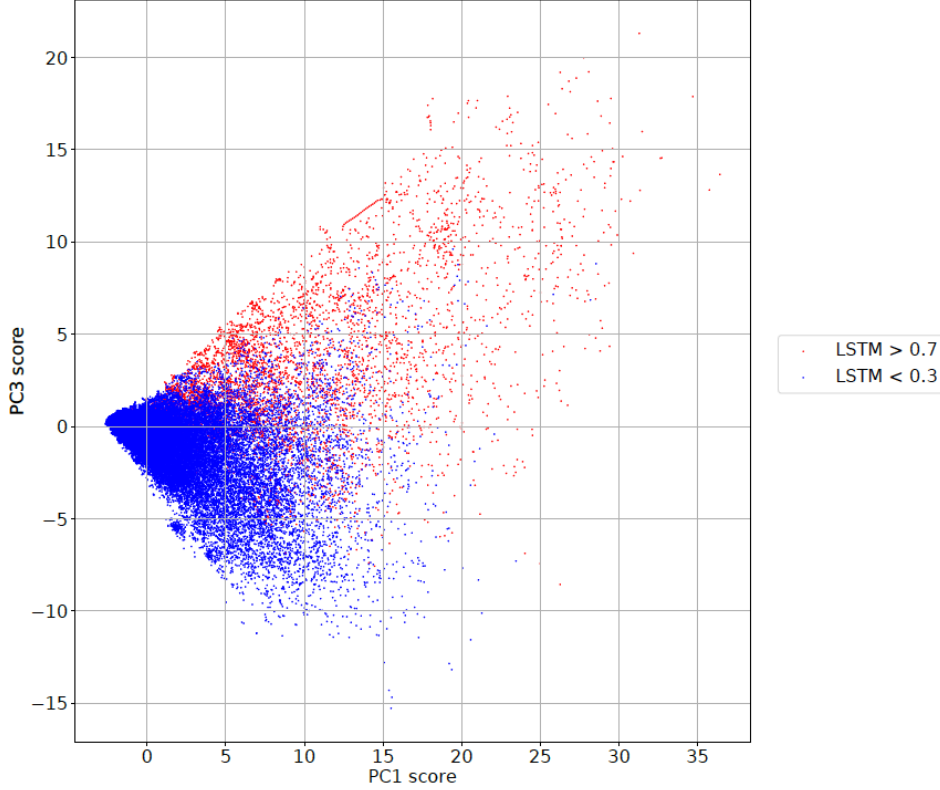


Figure 12. PC1 and PC3 score of cases where LSTM score greater than 0.7 (red) and lower than 0.3 (blue). We found that typically, inputs with LSTM score higher than 0.7 will have positive PC3 score, while inputs with score lower than 0.3 will have negative PC3 score.

To see the PC score dynamics for specific active region, we have plotted how PC1 and PC3 scores have evolved as time went by for four different active regions that have gone through sudden transition. Results are shown in Figure 13.

The dynamics of PC1 and PC3 score across time is shown in a series of connected arrows in the PC score subspace. Apart from showing how the PC1 and PC3 score change for every 12 minutes using arrows, we also indicated whether the change happened during the LSTM score sudden transition time by labelling all sudden transition periods' arrows in green.

It can be seen from Figure 13 that when LSTM score became very high after the transition, namely above 0.7, typically the active regions will have both high PC1 and PC3, as indicated by the red arrows on the upper right corner of each graph. And during the transition time, where the LSTM score began to jump from lower than 0.3 to higher than 0.7, the trajectory of the PC1 and PC3 score escaped the area around the origin and those with very negative PC3, and travelled towards the region where PC1 score is above 20 and PC3 is above 5, which are surely the outliers in the PC1-PC3 subspace shown in Figure 12.

To illustrate the process of sudden transitions with the original SHARP parameters instead of the DTW distance features, in Figure 14, we have shown the original TOTPOT, MEANSHR, TOTPOT_D, MEANSHR_D of AR 11158 and 11190. The blue band highlights the 1-hour time-series at the baseline time. The yellow and the green band

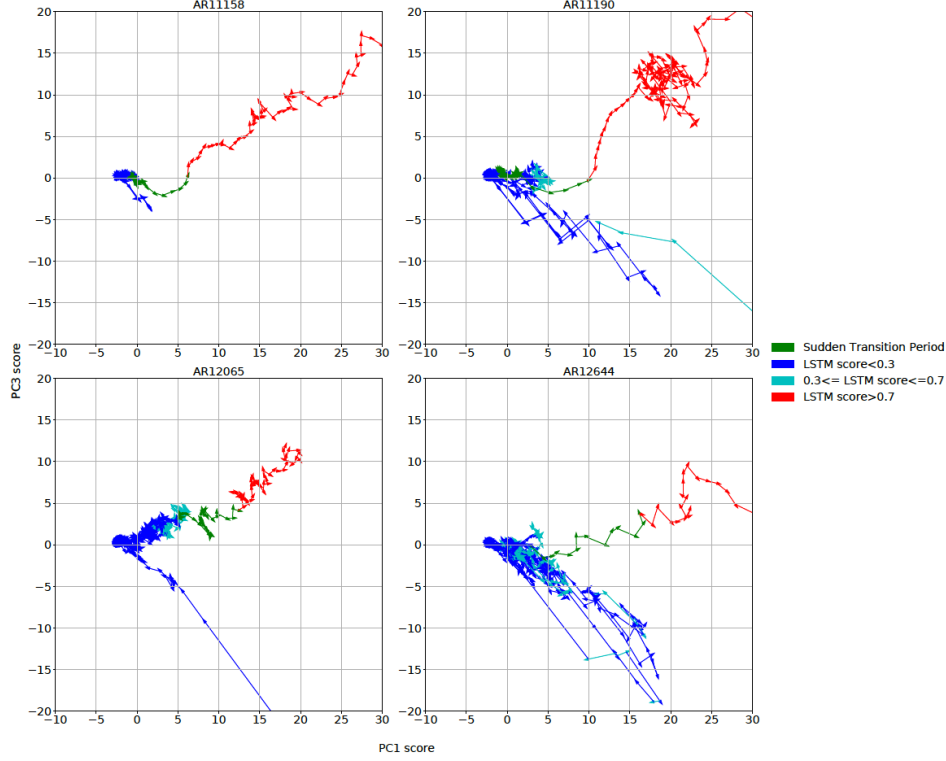


Figure 13. Four case studies on AR 11158, 11190, 12065 and 12644. Evolution path of PC1 and PC3 are plotted with connected arrows showing the direction of changes as time went by. Green arrows represent sudden transition period, where LSTM scores changed from very low (< 0.3) to very high (> 0.7). Other arrows are during the non-transition times, LSTM score below 0.3, between 0.3 and 0.7 and above 0.7 are colored blue, cyan and red, respectively. We found that: (i) during the sudden transition time, each active region’s PC1 and PC3 scores become further away from the origin and travelled towards the places where both PC scores are high. (ii) It seems that the location of the sudden transition period in the 2-d PC score space is similar across active regions, perhaps there exists a threshold in the PC space that separates low and high LSTM scores.

highlights a 3-hour time-series before and after the sudden transition of LSTM scores, featuring consistently low (<0.3) and high (>0.7) LSTM score.

It can be seen that the time-series before sudden transition is not very different from the baseline in all four quantities. But when LSTM score is very high, we could see an abrupt change of TOTPOT and MEANSHR inside the green band for both active regions. And the derivatives of TOTPOT is becoming very large, and the derivatives of MEANSHR has become super noisy. The general impression is that when LSTM scores higher, the main trend of the SHARP parameters have become very different from the baseline, and the signals of flare eruption has emerged. Additionally, the derivatives are becoming different from the baseline as well, with derivative of TOTPOT becomes higher, and derivative of MEANSHR becomes noisier.

In the case study of AR 11190 above, we could see that prior to the sudden transition time, there is another time (around 2011-04-12) where the LSTM score rises above zero but went back to zero before becoming very large. During this period, the TOT-

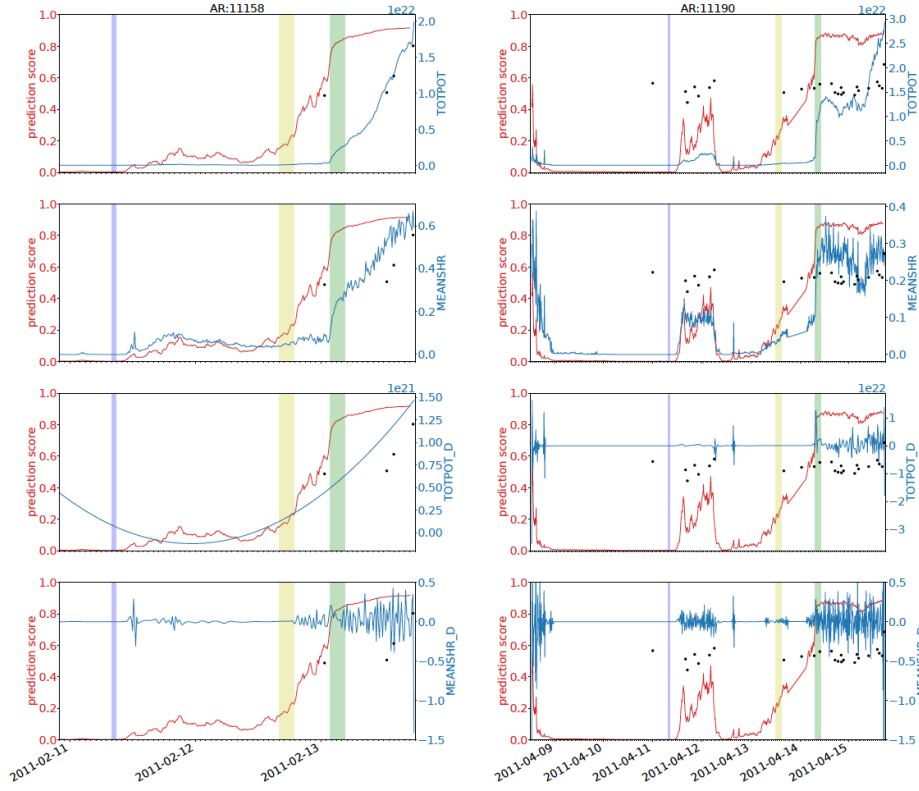


Figure 14. The original SHARP parameters TOTPOT, MEANSHR and their first-order time derivatives of AR 11158 and 11190. The blue band shows the 1-hour time-series chosen as the baseline for DTW distance calculation. The yellow and green band are a 3-hour time-series before and after the sudden transition of LSTM scores. Each small black dots stands for a recorded flare event. The height of the dot is proportional to the logarithm of flare intensity, which is the same as that in Figure 4. Minor ticks on the time axis are plotted for every hour. We could see that compared to time before transition and time at the baseline, the TOTPOT and MEANSHR time-series show more increasing trends after the sudden transition. And their first-order time derivative show more volatility than the low prediction score time. These are the driving forces behind the high PC1 and PC3 scores after their sudden transitions. Units of TOTPOT, TOTPOT_D, MEANSHR, MEANSHR_D are $\text{erg} \cdot \text{cm}^{-2}$, $\text{erg} \cdot \text{cm}^{-2} \cdot \text{h}^{-1}$, degree and degree $\cdot \text{h}^{-1}$. All parameters are weighted by the PIL mask.

POT only rises up mildly, but the MEANSHR has become significantly different from zero. This phenomenon is very common in the SHARP parameter dataset. One could see that during this time, there were several flares of intermediate intensities happening. The TOTPOT is not sensitive to these flares but only rises up before the last strong M/X flares. The MEANSHR, however, is more sensitive and could be fairly large even before these weaker flares. Such a sensitivity to weak flares sets the MEANSHR, and many other SHARP parameters about magnetic field gradients such as MEANGBT, MEANGBH and MEANGBZ, apart from the SHARP parameters that have are more insensitive to weaker flares, such as USFLUX, ABSNJZH, SAVNCP and TOTPOT.

PC3 is indeed capturing these insensitive features. It is giving all SHARP parameters such as TOTPOT, TOTUSJH, SAVNCP, USFLUX positive loadings but near zero loading for MEANSHR, MEANGAM and MEANGBH. Since MEANSHR, MEANGAM

and MEANGBH can become high even before some weak flares, they cannot help one to distinguish LSTM inputs before a C flare and an M flare as good as other SHARP parameters.

If we call the insensitive features such as TOTPOT as **signals**, and all the sensitive ones such as MEANSHR_D as **noise**, then PC1 is simply the signals plus noise, and PC3 is signal minus noise. The LSTM score will be high only when the signal features are very large. If we only observe large noise features, it can be the case that weak flares are happening. Such a SHARP parameter taxonomy echoes the finding on variable importance in Chen et al. (2019) where the accuracy of LSTM classification drops only a little if it is trained solely with TOTUSJH or TOTPOT, but drops a lot when trained solely with MEANSHR or MEANGAM.

The LSTM model is not able to handle signals and noises to perfection. This is because the noise features are becoming higher together with the signal features before an M/X flare. But before weak flares, it is more likely that we only see some noise features rising up. So the LSTM cannot tell which type of flare is going to happen under the cases when MEANSHR is very high and volatile, unless it sees some significant TOTPOT as well. As one can see from the case study of AR 11190 in Figure 14, a significantly non-zero MEANSHR still drives the LSTM score to nearly 0.4 during 2011-04-12 for AR 11190. But the LSTM is still able to pick up the true signals for strong flares. As the TOTPOT rises up for AR 11190, the LSTM score breaks the upper bound at 0.4 and soared to nearly unity.

In this subsection, we have summarized the information of DTW distance features into a few principal components. And we provided a visualization where we projected LSTM inputs into a 2-dimensional space. We highlighted a particular principal component, the PC3, that could separate the low and high LSTM cases. Case studies are used to demonstrate that the time evolution of some SHARP parameters have very different behaviors before weak flares and strong flares, such as the TOTPOT and all others with positive loadings in PC3. They are the true signals of strong flares picked up by LSTM model. There are other SHARP parameters, such as the MEANSHR, that have smaller contrasts before weak and strong flares. Such features might confuse the LSTM model when it is doing the classification of weak and strong flares. They introduce noises in LSTM inputs, and their derivatives have negative loadings in PC3.

The analysis in this section is still very qualitative. In the next subsection, we are going to find the exact threshold of PC scores and SHARP parameters that could split the low and high LSTM score cases. To make our analysis more quantitative, we will use decision tree and random forests to find the threshold value.

4.3 Tree-based method analysis on LSTM results

Classification and regression tree (CART) is a non-parametric statistics model that partitioned the feature space into several disjoint regions, and fits a model inside each region. It uses a tree-like structure consisting of decision nodes and leaves. Each decision node has one of the input features and an optimized split value. Any input data that has the feature above or below the split value would be passed down to different subtrees until a leaf node is reached. At the leaf node, CART will return a categorical (classification) or continuous (regression) fitted value. CART is fitted to minimize a certain loss function that describes the aggregated leaf node purity, and we used Gini-index in this paper. For a more comprehensive background on CART model, we recommend our readers to Hastie et al. (2001, Chapter 9.2).

CART is known to have low bias but overfits the data most of the time. To overcome the overfitting issue of CART, people either use tree-pruning or bagging. Tree-pruning is to reduce the depth of the decision tree to avoid having too many split values. Bag-

ging, or bootstrap aggregating, is to use bootstrap method to generate multiple training dataset and fit multiple models on each new training dataset. Final predictions or classifications are made based on the outputs of all fitted models.

Random forests (RF) is a bagging method that fits multiple tree-based models at the same time with bootstrapped samples and aggregates all outputs to give the final classification/regression output. Each tree in the RF is fitted independently with randomly-selected features that is a subset of all input features. Hastie et al. (2001, Chapter 15) provides a complete introduction to random forest method.

In the previous subsection, we have conducted a PCA analysis on our DTW distance features of 18 SHARP parameters and their 18 derivatives. And a general impression is that when PC1 and PC3 scores are becoming very high (in the upper right corner of each sub-figure in Figure 13), we could anticipate a high LSTM prediction score. In this subsection, we applied both pruned CART and random forests to our PCA scores and the DTW features of SHARP parameters to classify low (<0.3) and high (>0.7) LSTM score cases. We aim at using these models to find whether there are threshold values for certain PC score or DTW features of certain SHARP parameters. If one LSTM input surpassed the threshold, we could expect that the LSTM score is more likely to be high, as suggested by the pattern in (b) of Figure 6. To capture this notion precisely with CART, we calculated the PCA scores for all HARP regions' 36 DTW distance features, and we take the first 10 principal components' scores for each HARP region which have explained 88.6% of the total variations. As a result, for each LSTM score on a leave-one-out score path, we have associated it with a 10-dimensional PCA score. We have in total 141,350 PCA score-LSTM score pairs coming from the 360 score paths.

For each LSTM score, we label it as 1 if it is above 0.7, and label it as 0 if it is below 0.3, and drop it otherwise. Such a procedure leaves us 125,955 samples of 10-dimensional PCA scores with associated 0/1 class label. We will use CART to see which PC score could lead to high LSTM scores above 0.7 and low LSTM scores below 0.3. To construct a train set and a test set for the CART model, we split all samples based on the active region where the samples come from. The train-test split makes sure that all PC scores from the same HARP region will only appear in either train or test set. Eventually, we have obtained a train set with 84,220 samples including 2,755 high LSTM score cases and a test set with 41,735 samples, of which 2,419 cases have high LSTM scores.

Figure 15 shows the result of the classification tree using the top 10 principal components' scores with the tree's maximum depth limited to 3 to avoid too much overfitting.

The visualization of the classification tree follows a tree structure, with each rectangle box containing the information about the feature used at the node, the split value, the impurity of the node (Gini-index), the number of samples of each class remaining to be classified at the node and the majority of the samples' class at the current node. The top of the decision tree is the root node, and it is the first if-else statement of the whole tree. We could see that the root node splits at PC3 score at 1.112. All samples with PC3 score below this will be passed to the sub-tree on the left for further classification while all others will be passed to the sub-tree on the right. We could see that after just one thresholding of PC3 score, we have already obtained two sub-trees that have majority of the samples being low and high LSTM scores cases, as indicated by the color on the left and right branch after the root node splitting. The test set prediction accuracy of this classification tree is 89.3%.

Since our train test set split procedure could have some randomness regarding which active regions are put in the test set, we may have different variations of the tree if we have a slightly different composition of the train and test set. To evaluate whether PC3 score appears consistently at the root node and plays a key role in the thresholding, we

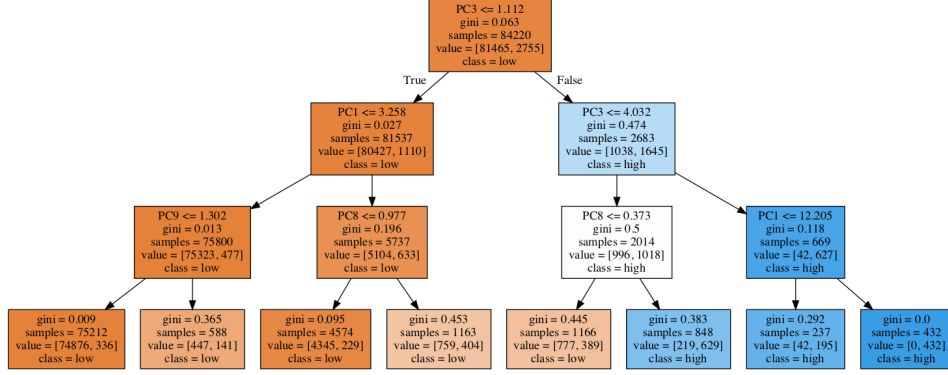


Figure 15. Classification Tree fitted using PCA scores to classify low and high LSTM score cases. In each rectangle box, there is a feature and a split value in the first line, such as $PC3 \leq 1.112$ in the first box. It means that for any sample, if this condition is satisfied, it will be passed down to the left branch, otherwise it will be passed to the right branch. All training samples will finally end up in a box at the bottom. Decision nodes with the majority of the samples being the low LSTM scores are colored in brown, and nodes with the majority of the samples being the high LSTM scores are colored in blue. The darkness of the colors represent the purity of the node. One can see that after thresholding all training samples with PC3 score at 1.112, the left sub-tree mainly consists of low LSTM score cases and the right sub-tree consists of high LSTM score cases. The PC3 score is a very good variable to set a threshold.

rerun the decision tree with maximum depth restricted to 3 for 100 times with different train and test set, and calculate the feature importance of each of the 10 PC scores in each iteration. Feature importance could be interpreted as the contribution of the feature to the classification. In each iteration, we rank all PCs by their feature importance and the top 3 PCs. It turns out that PC3 is always the most important feature, PC1 is the second most important feature most of the time. The left panel of Figure 16 shows the distribution of the test set prediction accuracy and the feature importance of the PC ranks 1st, 2nd, 3rd in each iteration’s feature importance ranking.

The PC3 is consistently the “Rank 1st PC” in terms of feature ranking in the 100 iterations. But at the same time, we could see that the feature importance of PC3 scores and others vary a lot, so does the test set precision, which ranged from less than 0.6 to nearly 1.0. To obtain more robust results, we used the random forests to do the classification of low and high LSTM scores with the PCA scores. With the same train-test set splitting procedure, we run the random forests with 50 trees, with each tree being a classification tree using up to 2 of the 10 PCA scores. And the classification result of the random forests is taking the majority of the results returned by the 50 trees. Similarly, we run the random forests with 100 iterations and plot the distribution of test set accuracy, feature importance of PC ranks 1st, 2nd and 3rd in each iteration’s feature importance ranking in the right panel of Figure 16. This time, PC3 is still the most important feature among all in all iterations, and PC1 ranks 2nd in 99 out of the 100 iterations.

All previous tree-based methods are applied to PCA scores. The results of both tree-based methods showed that the PC3 score consistently stands out as the most important feature compared to all other principal components. This confirms our previous result that when PC3 score is positive, it is very likely that the LSTM is predicting a strong flare. Simply speaking, PC3 contains the information of the signals that can predict strong flare eruption. We then apply the tree-based fitting model to the origi-

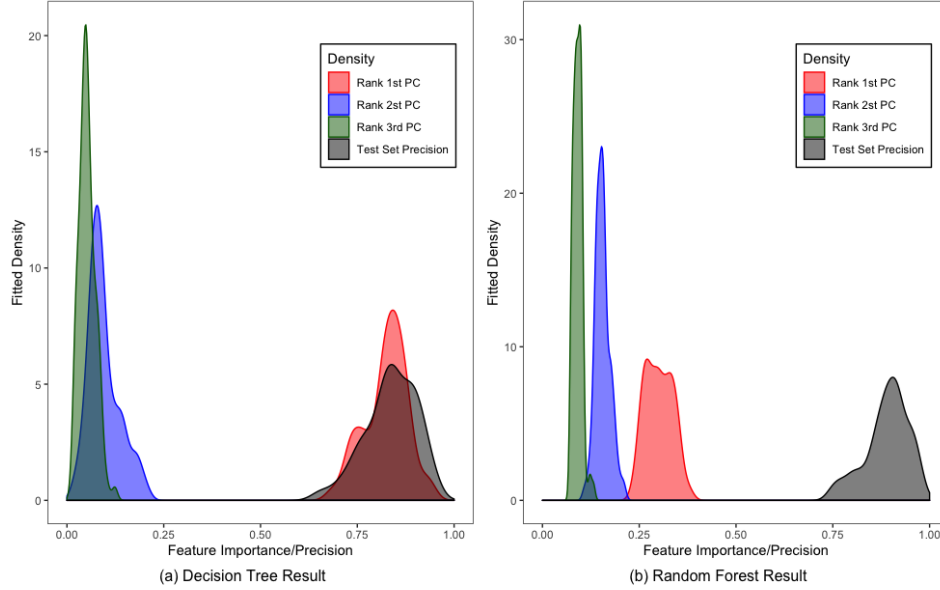


Figure 16. Results of Classification and regression tree (CART) and Random Forests, each with 100 iterations, with each iteration having a different train set and test set. Distributions of test set accuracy, feature importance of PC ranks 1st, 2nd and 3rd in each iteration’s feature importance ranking are plotted. In both models, the Rank 1st PC is PC3 in all iterations. PC1 is the Rank 2nd PC 62% of the time in decision tree and 99% of the time in random forests.

nal 18 SHARP parameters’ DTW distance features, and their associated time derivatives’ DTW distance features to directly evaluate each SHARP parameters’ association with the LSTM score in the same way as the 10 PCA scores. Figure 17 shows the result on the classification tree fitted on the DTW distance features with the same train set and test set as the ones used in generating Figure 15. Now, we find that by using the total free energy density (TOTPOT) as the root node feature and setting the split value to be $7.9 \times 10^{21} \text{ erg} \cdot \text{cm}^{-1}$ results in two sub-trees with a clear pattern. The left hand side sub-tree mainly consists of low LSTM score cases and the sub-tree on the right consists of high LSTM score cases. The decision tree has a precision of 91.2%.

Indeed, one can see that the second layer of the tree also uses TOTPOT as the decision node feature. And most of the train set cases with high LSTM scores have TOTPOT’s DTW distance feature above $2.25 \times 10^{21} \text{ erg} \cdot \text{cm}^{-1}$. If one uses Euclidean distance to approximate the DTW distance between two 1-hour TOTPOT time-series and assume that the baseline has very negligible ($= 0$ in all 5 frames) total free energy density, one could say that a threshold for the magnitude of total free energy density that could lead to high LSTM score is around $1.0 \times 10^{21} \text{ erg} \cdot \text{cm}^{-1}$. Note that the threshold should be interpreted as a PIL mask weighted parameter. This threshold works well for the case studies shown in Figure 14.

There is a caveat on interpreting TOTPOT’s importance in the decision tree in that there are many features that are highly correlated with TOTPOT that could have similar feature importance as that of TOTPOT has TOTPOT been taken away from the random forests’ inputs. So in general, one could conclude that the block of variables that are highly correlated with total free energy density can be used to establish some threshold values to distinguish cases with low and high LSTM scores. Once again, the decision tree analysis confirmed our previous statement that the signals picked up by LSTM model to predict strong solar flares are the SHARP parameters that are highly corre-

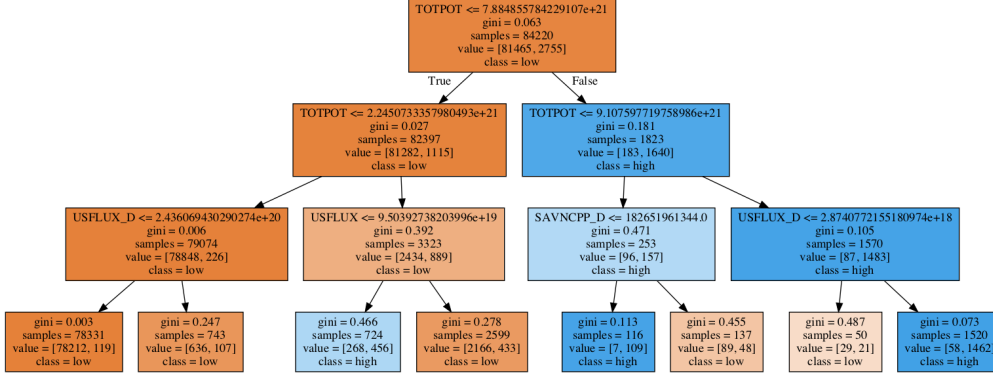


Figure 17. Classification Tree fitted using DTW distance features. Decision nodes with the majority of the samples being the low LSTM scores is colored in brown, and nodes with the majority of the samples being the high LSTM scores is colored blue. The darkness of the colors represent the purity of the node.

lated with total free energy density, including TOTUSJH, MEANJZH, MEANALP, TOTPOT, MEANPOT, TOTUSJZ, ABSNJZH, SAVNCPD, and USFLUX.

Generally speaking, our tree-based analysis on DTW distance features showed that when the 1-hour total free energy density time-series input into the LSTM, or other highly correlated variables' 1-hour time-series, become extremely different from the baseline 1-hour time-series of the HARP region, it is associated with high LSTM scores. Our results based on the PCA scores demonstrated that there are the two groups of variables, one with high positive loadings in PC3 (signals), the other with high negative loadings in PC3 (noises), that play a key role out of all features in separating low and high LSTM score cases.

5 Discussion and Conclusion

Our paper presents the results and interpretations of Long-Short-Term-Memory (LSTM) model's predictions of first flares using the parameters calculated from Space-weather HMI Active Region Patches (SHARPs) where parameters are calculated along the polarity inversion line (PIL). Specifically, we trained LSTM model to distinguish B first flares against M/X first flares and have generated a prediction score path for 360 active region's first flares, among which we found 35 regions' first M/X flare has a sudden transition of LSTM score prior to the flare eruption. On average, the sudden transition completed 48 hours before the flare. The rapid transition provides a unique opportunity to interpret the LSTM model and determine which physical features represented by the SHARP parameters drive the flare prediction.

To interpret LSTM predictions, we propose a two-step method to project LSTM's matrix-shaped inputs into a low dimensional space. In the first step, we utilize dynamic time warping (DTW) to measure the temporal dimension similarity of any two LSTM inputs. And by picking a specific LSTM input, the baseline LSTM input, as a benchmark, we managed to collapse the information of LSTM input matrices into a low dimensional DTW distance vector. We further reduce the dimensions in the second step by PCA. Finally, we construct a feature, the PC3, that linearly combines the similarity metric of each SHARP parameter and their derivatives. By examination of active regions experiencing a sudden transitions of LSTM prediction scores, and tree-based classification, we find that the PC3 can well separate LSTM inputs that give low and high

prediction scores. A careful inspection of the two representative features, total free energy density (TOTPOT) and mean shear angle (MEANSHR), shows that the LSTM learns strong flare eruptions out of a few features that carry strong signals, which frequently increase before the strong flare occurs. PC3 gives the signals strong positive loadings, which reflects the learning pattern of LSTM. The interpretation of LSTM highlights that TOTPOT and those highly correlated SHARP parameters contain the key indicators of strong flare eruption. While the SHARP parameters highly correlated with the MEANSHR can introduce noises into the LSTM model in the sense that they can be more volatile not only during the strong flare time, but also weak flare time and even quiet times.

The interpretation of the LSTM results allows us to identify key photospheric signatures of the energy buildup leading to flares. To give some idea of the complexity of behavior, we have shown two representative examples where the probability of a large (M/X-class) flare rises in tandem with the buildup of total free energy (TOTPOT) and mean magnetic shear (MEANSHR) relative to pre-event baselines. In the case of AR 12017, the probability peaks with a rapid rise in free energy (and DTW) that levels off near the flare-time level. Here, the LSTM model near certain prediction of a large flare corresponds with levels of free energy that implies it is only a matter of time before a major flare will occur. In other words, it is very unlikely that the system can relax without the occurrence of a large flare. In the case of AR 12381, the probability of a major flare becomes high while the total free energy is increasing but still well below the flare-time level. This example shows that the model can identify a trend of increasing free energy that is likely to continue to culminate in a flare. The contrast in examples that there are distinct evolutionary paths leading to flares, each of which has unique baseline to gauge the necessary energy requirements. We find a threshold for the magnitude of total free energy density that produces a high probability of a flare is around 1.0×10^{21} erg \cdot cm $^{-1}$.

Free energy is a necessity for solar eruptions, and fixed thresholds for initiation have been proposed (Moore et al., 2012). The LSTM identifies the free energy and mean magnetic shear as critical variables for predicting flares. This result reflects the extraordinary complexity and varying structure of ARs, that are governed by common physical processes. The nature of those processes are elucidated by the role of the mean magnetic shear in the flare predictions. The mean shear is a measure of the non-potential nature of the magnetic field and in these circumstances indicates that the photospheric magnetic field is oriented nearly parallel to the polarity inversion line (PIL) (in contrast to a potential field, which would be perpendicular to the PIL). The sheared magnetic configuration is nearly universally observed in association with solar eruptions and our work confirms its essential role in large flares. Several leading theories offer different explanations for this magnetic shear such as sunspot collisions (Fang & Fan, 2015), rotating motion in super granules (Antiochos, 2013) and magnetic flux emergence (W. Manchester, 2003; W. Manchester IV et al., 2004; W. Manchester IV, 2007). In a followup paper, we will analyze the HMI vector magnetograph data for these 35 active regions and determine in detail how the the magnetic shear developed, and physical processes responsible for the buildup of energy leading to the first M/X-class flares.

Our post-hoc analysis has provided extra insights about solar flare predictions with machine learning model. Following the discussions in Chen et al. (2019), we advanced our understanding about machine learning predictions in the following aspects:

- We used SHARP parameters calculated along the polarity inversion line instead of the the ones calculated from the full HMI images to train LSTM model.
- We identified 35 active regions with sudden transitions of LSTM scores and have done case studies only on these selected active regions with the sharpest prediction score contrast.
- We have proposed a dimension-reduction technique based on dynamic time warping (DTW) and principal component analysis (PCA) to summarize the informa-

tion contained in matrix-shaped LSTM inputs. The low-dimensional representation of LSTM inputs shows some very interpretable learning patterns of LSTM model.

- Constructed features in the low-dimensional space still have very good interpretability, and we showed that the key feature contains signals from a subset of SHARP parameters and noises from others.
- Specifically, we showed that SHARP parameters that are highly correlated with total free energy density are the important signals for strong flare eruption learnt by the LSTM model. On the contrary, SHARP parameters whose derivatives are highly correlated with the derivative of mean shear angle introduce noises to the flare eruption pattern learnt by the LSTM model.
- A threshold for total free energy density along the polarity inversion line at $1.0 \times 10^{21} \text{ erg} \cdot \text{cm}^{-1}$ is given, surpassing which indicates that a strong flare is about to happen.

Appendix A Summary of Sudden Transition Cases

AR Number	Prior Transition Time	Post Transition Time	Flare Time
11410	2012-02-04 14:00:00	2012-02-06 02:48:00	2012-02-06 20:00:00
11560	2012-08-30 10:00:00	2012-08-30 14:12:00	2012-09-06 04:13:00
11613	2012-11-12 03:00:00	2012-11-12 04:12:00	2012-11-12 23:28:00
11618	2012-11-19 18:00:00	2012-11-20 09:00:00	2012-11-20 19:28:00
11718	2013-04-09 03:12:00	2013-04-11 05:24:00	2013-04-12 20:38:00
11726	2013-04-20 00:36:00	2013-04-20 06:00:00	2013-04-22 10:29:00
11762	2013-06-01 16:36:00	2013-06-02 21:12:00	2013-06-05 08:57:00
11817	2013-08-11 07:12:00	2013-08-12 00:12:00	2013-08-12 10:41:00
11818	2013-08-13 08:48:00	2013-08-14 17:24:00	2013-08-17 18:24:00
11861	2013-10-10 19:36:00	2013-10-11 04:12:00	2013-10-17 15:41:00
11891	2013-11-06 21:24:00	2013-11-07 02:12:00	2013-11-08 09:28:00
11928	2013-12-18 21:12:00	2013-12-19 05:12:00	2013-12-22 08:11:00
11153	2011-02-08 08:24:00	2011-02-08 13:36:00	2011-02-09 01:31:00
11968	2014-01-30 06:36:00	2014-01-30 15:36:00	2014-01-31 15:42:00
11158	2011-02-12 18:48:00	2011-02-13 01:48:00	2011-02-13 17:38:00
12017	2014-03-28 01:00:00	2014-03-28 03:36:00	2014-03-28 19:18:00
11165	2011-03-05 19:48:00	2011-03-06 01:12:00	2011-03-07 07:54:00
11169	2011-03-09 03:36:00	2011-03-09 19:24:00	2011-03-14 19:52:00
12065	2014-05-24 01:36:00	2014-05-24 08:24:00	2014-05-24 18:35:00
12085	2014-06-07 17:00:00	2014-06-08 17:48:00	2014-06-12 09:37:00
12089	2014-06-11 04:00:00	2014-06-11 13:24:00	2014-06-12 20:03:00
12182	2014-10-02 23:00:00	2014-10-03 02:48:00	2014-10-09 01:43:00
11190	2011-04-13 14:48:00	2011-04-14 07:24:00	2011-04-15 17:12:00
12257	2015-01-08 19:36:00	2015-01-09 09:00:00	2015-01-13 04:24:00
12280	2015-02-04 13:48:00	2015-02-05 01:36:00	2015-02-09 23:35:00
12360	2015-06-11 07:12:00	2015-06-11 16:36:00	2015-06-13 07:29:00
12381	2015-07-05 12:36:00	2015-07-06 00:36:00	2015-07-06 08:44:00
12403	2015-08-18 10:48:00	2015-08-18 11:48:00	2015-08-21 02:18:00
12423	2015-09-27 12:48:00	2015-09-27 18:24:00	2015-09-28 03:55:00
12422	2015-09-25 06:48:00	2015-09-26 09:12:00	2015-09-27 10:40:00
12644	2017-04-01 13:24:00	2017-04-01 15:48:00	2017-04-01 21:48:00
11260	2011-07-25 22:00:00	2011-07-26 03:36:00	2011-07-27 16:07:00
11261	2011-07-28 15:00:00	2011-07-29 09:24:00	2011-07-30 02:09:00
11263	2011-07-30 10:12:00	2011-07-31 15:36:00	2011-08-03 04:32:00
11283	2011-09-04 03:36:00	2011-09-04 11:48:00	2011-09-06 01:50:00

Table A1. Active regions with sudden transitions of LSTM prediction scores. Each row contains the information of the active region number, the time before and after the sudden transition and the first M/X flare time. All times are in the format Year-Month-Day Hour-Minutes-Seconds. On average, the sudden transition completed 48 hours before the flare.

Acknowledgments

We thank Yang Liu from Solar Dynamics Observatory (SDO) of Stanford University, Meng Jin from Lockheed Martin and Alfred Hero from University of Michigan for very useful comments on the data and statistics analysis of our paper. We really appreciate the help on the data preparation of the polarity inversion line based SHARP parameters by Jingjing Wang from National Space Science Center in Beijing.

References

- Antiochos, S. K. (2013, Jul). Helicity Condensation as the Origin of Coronal and Solar Wind Structure. *Astrophysical Journal*, *772*(1), 72. doi: 10.1088/0004-637X/772/1/72
- Aulanier, G., Török, T., Démoulin, P., & DeLuca, E. E. (2010, January). Formation of Torus-Unstable Flux Ropes and Electric Currents in Erupting Sigmoids. *Astrophysical Journal*, *708*, 314-333. doi: 10.1088/0004-637X/708/1/314
- Bishop, C. M. (2006). *Pattern recognition and machine learning*. Springer Science+Business Media.
- Bobra, M. G., & Couvidat, S. (2015). Solar flare prediction using SDO/HMI vector magnetic field data with a machine-learning algorithm. *Astrophysical Journal*, *798*(2), 135.
- Bobra, M. G., Sun, X., Hoeksema, J. T., Turmon, M., Liu, Y., Hayashi, K., . . . Leka, K. D. (2014, Sep 01). The helioseismic and magnetic imager (hmi) vector magnetic field pipeline: Sharps – space-weather hmi active region patches. *Solar Physics*, *289*(9), 3549–3578.
- Camporeale, E. (2019). The challenge of machine learning in space weather: Nowcasting and forecasting. *Space Weather*, *17*(8), 1166-1207.
- Canfield, R. C., Hudson, H. S., & McKenzie, D. E. (1999, March). Sigmoidal morphology and eruptive solar activity. *Journal Geophysical Research*, *26*, 627-630. doi: 10.1029/1999GL900105
- Chen, Y., Manchester, W. B., Hero, A. O., Toth, G., DuFumier, B., Zhou, T., . . . Gombosi, T. I. (2019). Identifying solar flare precursors using time series of sdo/hmi images and sharp parameters. *Space Weather*, *0*(0). Retrieved from <https://agupubs.onlinelibrary.wiley.com/doi/abs/10.1029/2019SW002214> doi: 10.1029/2019SW002214
- Dove, J. B., Gibson, S. E., Rachmeler, L. A., Tomczyk, S., & Judge, P. (2011, Apr). A Ring of Polarized Light: Evidence for Twisted Coronal Magnetism in Cavities. *Astrophysical Journal Letters*, *731*(1), L1. doi: 10.1088/2041-8205/731/1/L1
- Falconer, D. A., Gary, G. A., Moore, R. L., & Porter, J. G. (2000, Jan). An Assessment of Magnetic Conditions for Strong Coronal Heating in Solar Active Regions by Comparing Observed Loops with Computed Potential Field Lines. *Astrophysical Journal*, *528*(2), 1004-1014. doi: 10.1086/308188
- Falconer, D. A., Moore, R. L., & Gary, G. A. (2002, April). Correlation of the Coronal Mass Ejection Productivity of Solar Active Regions with Measures of Their Global Nonpotentiality from Vector Magnetograms: Baseline Results. *Astrophysical Journal*, *569*, 1016-1025. doi: 10.1086/339161
- Falconer, D. A., Moore, R. L., & Gary, G. A. (2003, October). A measure from line-of-sight magnetograms for prediction of coronal mass ejections. *Journal Geophysical Research*, *108*, 1380. doi: 10.1029/2003JA010030
- Falconer, D. A., Moore, R. L., & Gary, G. A. (2006, June). Magnetic Causes of Solar Coronal Mass Ejections: Dominance of the Free Magnetic Energy over the Magnetic Twist Alone. *Astrophysical Journal*, *644*, 1258-1272. doi: 10.1086/503699
- Fang, F., & Fan, Y. (2015, Jun). δ -Sunspot Formation in Simulation of Active-region-scale Flux Emergence. *Astrophysical Journal*, *806*(1), 79. doi: 10.1088/

0004-637X/806/1/79

- Forbes, T. G. (2000, October). A review on the genesis of coronal mass ejections. *Journal of Geophysical Research*, *105*, 23153-23166. doi: 10.1029/2000JA000005
- Georgoulis, M. K., Titov, V. S., & Mikić, Z. (2012, Dec). Non-neutralized Electric Current Patterns in Solar Active Regions: Origin of the Shear-generating Lorentz Force. *Astrophysical Journal*, *761*(1), 61. doi: 10.1088/0004-637X/761/1/61
- Green, L. M., Kliem, B., & Wallace, A. J. (2011, February). Photospheric flux cancellation and associated flux rope formation and eruption. *Astronomy and Astrophysics*, *526*, A2+. doi: 10.1051/0004-6361/201015146
- Green, L. M., Török, T., Vršnak, B., Manchester, W., & Veronig, A. (2018, Feb). The Origin, Early Evolution and Predictability of Solar Eruptions. *Space Science Reviews*, *214*(1), 46. doi: 10.1007/s11214-017-0462-5
- Hastie, T., Tibshirani, R., & Friedman, J. (2001). *The elements of statistical learning*. New York, NY, USA: Springer New York Inc.
- Hochreiter, S., & Schmidhuber, J. (1997). Long short-term memory. *Neural computation*, *9*(8), 1735–1780.
- Hoeksema, J. T., Liu, Y., Hayashi, K., Sun, X., Schou, J., Couvidat, S., ... Turmon, M. (2014, September 01). The helioseismic and magnetic imager (HMI) vector magnetic field pipeline: Overview and performance. *Solar Physics*, *289*(9), 3483–3530.
- Huang, X., Wang, H., Xu, L., Liu, J., Li, R., & Dai, X. (2018, Mar). Deep Learning Based Solar Flare Forecasting Model. I. Results for Line-of-sight Magnetograms. *Astrophysical Journal*, *856*(1), 7. doi: 10.3847/1538-4357/aae00
- Janvier, M., Aulanier, G., Bommier, V., Schmieder, B., Démoulin, P., & Pariat, E. (2014, Jun). Electric Currents in Flare Ribbons: Observations and Three-dimensional Standard Model. *Astrophysical Journal*, *788*(1), 60. doi: 10.1088/0004-637X/788/1/60
- Leka, K., & Barnes, G. (2018). Solar flare forecasting: Present methods and challenges. In N. Buzulukova (Ed.), *Extreme events in geospace* (pp. 65 – 98). Elsevier. doi: 10.1016/B978-0-12-812700-1.00003-0
- Leka, K. D., & Barnes, G. (2003a, oct). Photospheric magnetic field properties of flaring versus flare-quiet active regions. i. data, general approach, and sample results. *Astrophysical Journal*, *595*(2), 1277–1295. doi: 10.1086/377511
- Leka, K. D., & Barnes, G. (2003b, October). Photospheric Magnetic Field Properties of Flaring versus Flare-quiet Active Regions. II. Discriminant Analysis. *Astrophysical Journal*, *595*, 1296-1306. doi: 10.1086/377512
- Liu, C., Deng, N., Wang, J. T. L., & Wang, H. (2017, Jul). Predicting Solar Flares Using SDO/HMI Vector Magnetic Data Products and the Random Forest Algorithm. *Astrophysical Journal*, *843*(2), 104. doi: 10.3847/1538-4357/aa789b
- Lundberg, S. M., & Lee, S.-I. (2017). A unified approach to interpreting model predictions. In *Advances in neural information processing systems* (pp. 4765–4774).
- Magara, T., & Longcope, D. W. (2003, March). Injection of Magnetic Energy and Magnetic Helicity into the Solar Atmosphere by an Emerging Magnetic Flux Tube. *Astrophysical Journal*, *586*, 630-649. doi: 10.1086/367611
- Manchester, W. (2003, April). Buoyant disruption of magnetic arcades with self-induced shearing. *Journal of Geophysical Research (Space Physics)*, *108*, 1162. doi: 10.1029/2002JA009252
- Manchester, W., IV. (2007, September). Solar Atmospheric Dynamic Coupling Due to Shear Motions Driven by the Lorentz Force. *Astrophysical Journal*, *666*, 532-540. doi: 10.1086/520493
- Manchester, W., IV, Gombosi, T., DeZeeuw, D., & Fan, Y. (2004, July). Eruption of a Buoyantly Emerging Magnetic Flux Rope. *Astrophysical Journal*, *610*, 588-

596. doi: 10.1086/421516
- Moore, R. L., Falconer, D. A., & Sterling, A. C. (2012, May). The Limit of Magnetic-shear Energy in Solar Active Regions. *Astrophysical Journal*, 750(1), 24. doi: 10.1088/0004-637X/750/1/24
- Muranushi, Y. H., Muranushi, T., Asai, A., Okanohara, D., Raymond, R., Watanabe, G., ... Shibata, K. (2016). A deep-learning approach for operation of an automated realtime flare forecast. *CoRR*, abs/1606.01587. Retrieved from <http://arxiv.org/abs/1606.01587>
- Nishizuka, N., Sugiura, K., Kubo, Y., Den, M., & Ishii, M. (2018). Deep flare net (defn) model for solar flare prediction. *Astrophysical Journal*, 858(2), 113.
- Nishizuka, N., Sugiura, K., Kubo, Y., Den, M., Watari, S., & Ishii, M. (2017, jan). Solar flare prediction model with three machine-learning algorithms using ultraviolet brightening and vector magnetograms. *Astrophysical Journal*, 835(2), 156. doi: 10.3847/1538-4357/835/2/156
- Sakoe, H., & Chiba, S. (1978). Dynamic programming algorithm optimization for spoken word recognition. *IEEE Transactions on Acoustics, Speech, and Signal Processing*, 26(1), 43-49.
- Salvador, S., & Chan, P. (2007). Toward accurate dynamic time warping in linear time and space. *Intelligent Data Analysis*, 11(5), 561-580.
- Sander, J., Ester, M., Kriegel, H.-P., & Xu, X. (1998, Jun 01). Density-based clustering in spatial databases: The algorithm gbscan and its applications. *Data Mining and Knowledge Discovery*, 2(2), 169-194.
- Schmieder, B., Aulanier, G., & Vršnak, B. (2015, Dec). Flare-CME Models: An Observational Perspective (Invited Review). *Solar Physics*, 290(12), 3457-3486. doi: 10.1007/s11207-015-0712-1
- Schou, J., Scherrer, P. H., Bush, R. I., Wachter, R., Couvidat, S., Rabello-Soares, M. C., ... Tomczyk, S. (2012, January). Design and ground calibration of the helioseismic and magnetic imager (hmi) instrument on the solar dynamics observatory (sdo). *Solar Physics*, 275(1-2), 229-259.
- Schrijver, C. J. (2007, jan). A characteristic magnetic field pattern associated with all major solar flares and its use in flare forecasting. *Astrophysical Journal*, 655(2), L117-L120.
- Schrijver, C. J. (2009, Mar). Driving major solar flares and eruptions: A review. *Advances in Space Research*, 43(5), 739-755. doi: 10.1016/j.asr.2008.11.004
- Su, J., Liu, Y., Liu, J., Mao, X., Zhang, H., Li, H., ... Xie, W. (2008, Oct). Lorentz Force: A Possible Driving Force for Sunspot Rotation. *Solar Physics*, 252(1), 55-71. doi: 10.1007/s11207-008-9236-2
- Sun, X., Hoeksema, J. T., Liu, Y., Wiegmann, T., Hayashi, K., Chen, Q., & Thalmann, J. (2012, Apr). Evolution of Magnetic Field and Energy in a Major Eruptive Active Region Based on SDO/HMI Observation. *Astrophysical Journal*, 748(2), 77. doi: 10.1088/0004-637X/748/2/77
- Tziotziou, K., Georgoulis, M. K., & Raouafi, N.-E. (2012, Nov). The Magnetic Energy-Helicity Diagram of Solar Active Regions. *Astrophysical Journal Letters*, 759(1), L4. doi: 10.1088/2041-8205/759/1/L4
- Vemareddy, P., Ambastha, A., & Maurya, R. A. (2012, Dec). On the Role of Rotating Sunspots in the Activity of Solar Active Region NOAA 11158. *Astrophysical Journal*, 761(1), 60. doi: 10.1088/0004-637X/761/1/60
- Wang, H., Liu, C., Ahn, K., Xu, Y., Jing, J., Deng, N., ... Cao, W. (2017, Mar). High-resolution observations of flare precursors in the low solar atmosphere. *Nature Astronomy*, 1, 0085. doi: 10.1038/s41550-017-0085
- Wang, J., Liu, S., Ao, X., Zhang, Y., Wang, T., & Liu, Y. (2019, oct). Parameters derived from the SDO/HMI vector magnetic field data: Potential to improve machine-learning-based solar flare prediction models. *Astrophysical Journal*, 884(2), 175.
- Wang, R., Liu, Y. D., Hoeksema, J. T., Zimovets, I. V., & Liu, Y. (2018, Dec).

Roles of Photospheric Motions and Flux Emergence in the Major Solar Eruption on 2017 September 6. *Astrophysical Journal*, 869(2), 90. doi: 10.3847/1538-4357/aaed48

Witten, D. M., & Tibshirani, R. (2010). A framework for feature selection in clustering. *Journal of the American Statistical Association*, 105(490), 713–726.